CHALMERS

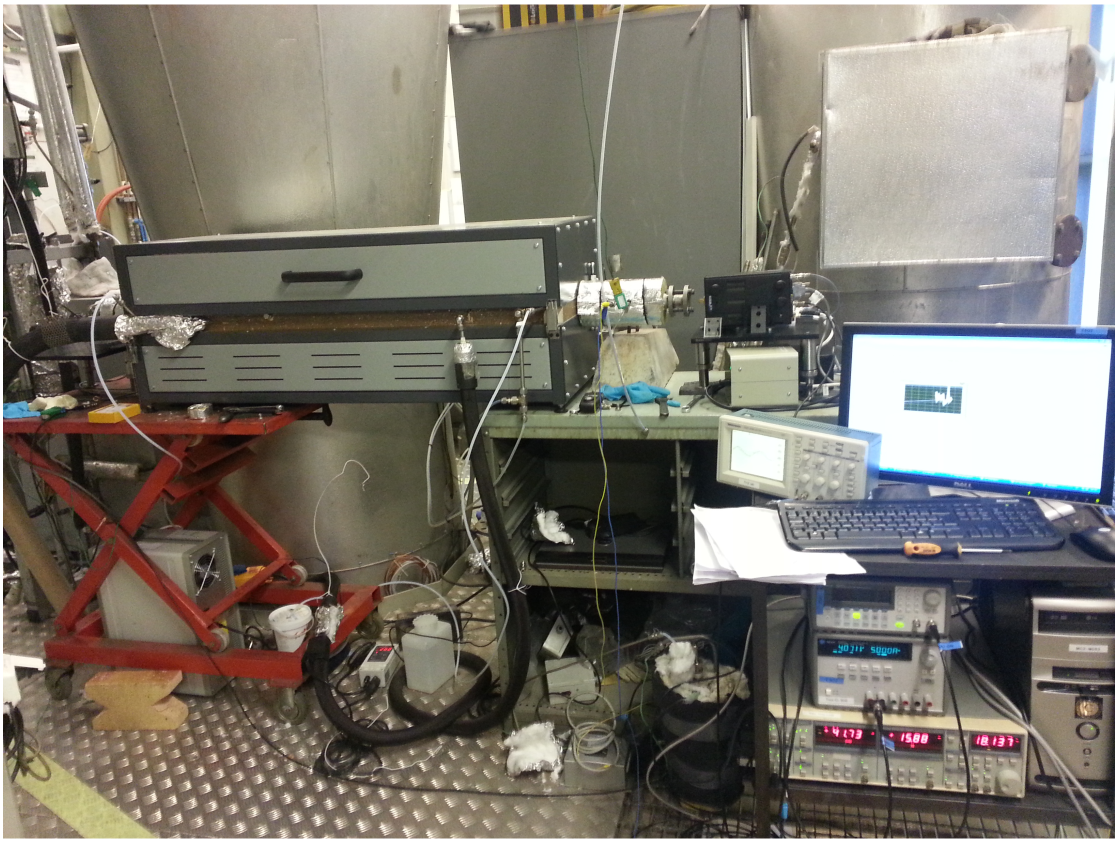

Online Detection of Water Vapor in an Industrial Gasifier Using Terahertz Spectroscopy

Master's Thesis in Physics and Astronomy

JENS NORDMARK

Department of Microtechnology and Nanoscience
Terahertz and Millimeter-wave Laboratory
Chalmers University of Technology
Gothenburg, Sweden 2013

Online Detection of Water Vapor in an Industrial Gasifier Using Terahertz Spectroscopy
Jens Nordmark

Terahertz and millimeter wave laboratory
Department of Microtechnology and Nanoscience
Chalmers University of Technology
SE-412 96 Gothenburg
Sweden

Abstract

A terahertz spectrometer was set up for the monitoring of product gas in a thermal gasifier. The goal was to measure temperature and H_2O concentration, and preferably also CO concentration. This environment presents several difficulties such as high temperature, toxic gases, high H_2O content and a high concentration of particulate pollutants. Spectroscopy using IR Lasers tend to be obstructed by the high absorption of H_2O as well as the scattering by the particulates, and so does not produce satisfactory results. It was hoped that these problems could be avoided by using terahertz radiation, with a lower absorption by water and a longer wavelength possibly avoiding scattering by particulates. A system operating in the range 300-500 GHz was built and tested in laboratory as well as in an industrial gasifier at Chalmers Power center, yielding promising results.

Our results indicate that monitoring of H_2O, and probably other gases, in the rugged environment of gasifier rawgas can be done with response times on the order of a few minutes. This has applications in biomass gasification, where variable quality of the fuel results in a need for continous monitoring and tuning of the gasification process.

Keywords: Terahertz, Gas spectroscopy, Gasification

Acknowledgements

I wish to thank my supervisor Sergey Cherednichenko for his help. I also wish to thank Hosein Bidgoli and Martin Seeman at the department for energy and the environment with whom the project was carried out. Also thanks to Johannes Öhlin for assistance during experiments at the Chalmers power center.

Jens Nordmark, Gothenburg July 1, 2013

Contents

List of Tables

List of Figures

Nomenclature

CH_4	Methane
CO	Carbon monoxide
CO_2	Carbon dioxide
H_2	Hydrogen
RH	Relative Humidity, ratio of H_2O partial pressure to saturated vapor pressure.
VMR	Volume Mixing Ratio
AMC	Amplifier-/Multiplier Chain
EM	Electromagnetism, Electromagnetic
GPIB	General purpose interface bus, same as IEEE 488
HITRAN	high-resolution transmission molecular absorption database
IEEE	Institute of Electrical and Electronics Engineers
IEEE 488	General purpose interface bus, GPIB
IR	Infrared
LINEPAK	Software library for spectral simulation described in Gordley et al. [1994].
NEP	Noise Equivalent Power
RMSD	Root Mean Square Deviation
SNG	Substitute Natural Gas, methane
tar	A loosely defined viscous black substance consisting mainly of large hydrocarbons, often aromatic, polycyclic and containing various substituents.
THz	TeraHertz
TTL	Transistor-Transistor Logic, a binary logic scheme using 0-0.8 V signals for low and 2.2-5 V for high

1

Introduction

Gasification of biomass is a technology expected to become more important as fossil fuels are to be replaced by carbon neutral bioenergy. The company WSP has made projections based on three scenarios, showing a potential for up to 12 TWh in biogas production by thermal gasification up to 2030 under favorable conditions. Distribution of the combustible gas produced (typically SNG, i.e. methane) could take place using the present natural gas infrastructure (Dahlgren et al. [2013]).

The properties of the fuels used are however such that the producer gas, also called rawgas in the stage immediately after it is generated, is full of char particles at sizes up to about one micron. At the same time its gas contents vary in time, and need to be tracked to tune the process. The particulate contents as well as the high H_2O content disturb the IR-spectroscopy that would typically be used to monitor gas content. H_2O simply has to high absorption in the IR for such radiation to be used successfully. The wavelength of IR is also at the order of the particulates diameter, giving rise to scattering that disrupts measurements. Gas chromatography is another technique traditionally used, but it cannot handle gas mixtures containing H_2O, which condenses in the chromatograph and destroys it. It is possible to measure the dry gas composition by first drying and cleaning the gas. This also provides a way to determine the sum of H_2O and tar contents, but only the total content and not both independently. In addition, it only works with a time delay of tens of minutes.

As an alternative solution, this project aimed to use terahertz spectroscopy in the hope to escape the aforementioned problems. Our aim was to measure content of H_2O as well as CO, one of the dry gases present. Our results indicate that this approach does work as desired.

There are several reasons why this approach succeeds. THz has a lower absorption for H_2O, avoiding saturation of the spectral lines. THz has longer wavelengths than IR, which reduces the scattering by particulates. The scattering of radiation by ideal spherical particles is described by Mie theory, where a threshold in the scattering cross

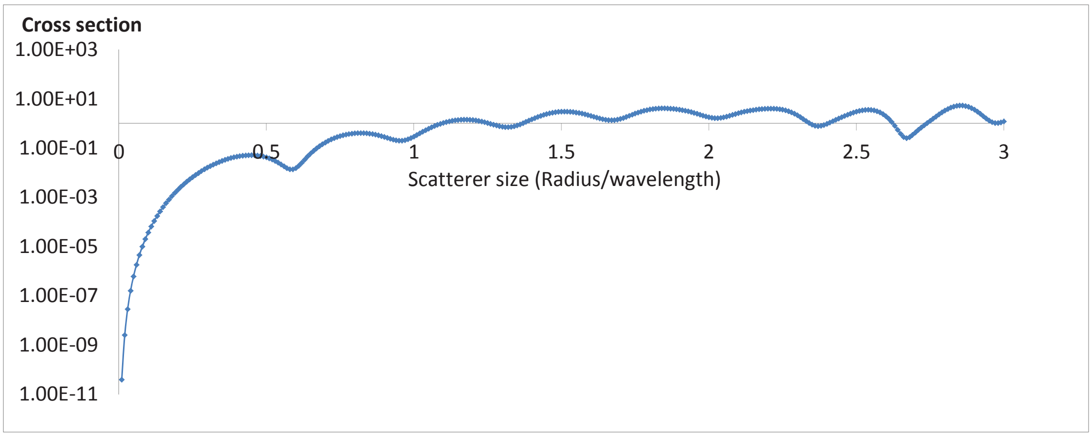

Figure 1.1: Scattering cross-section as function of $f_{\mathrm{rel}} = R/\lambda$ for a spherical particle. Calculated with MiePlot 4.3 by Laven [2013], implementing the BHMIE algorithm by Bohren and Huffman [2007]. [data/mie]

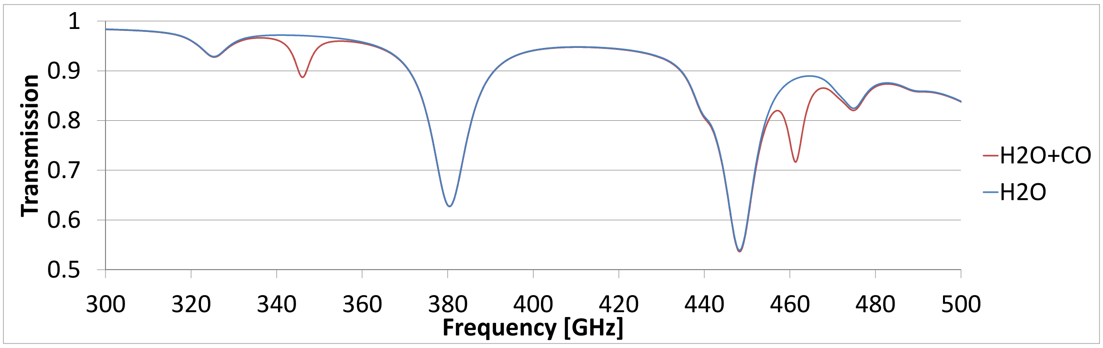

Figure 1.2: The spectra of two gas mixtures at room temperature (296 K). 10% H_2O (blue) and 10% H_2O+10% CO (red). [data/introspectrum]

section appears when the wavelength is comparable to the size of the scatterers, which can be formulated in terms of the relative frequency $f_{\mathrm{rel}} = R/\lambda \approx 1/2$ as shown in figure 1.1. In the low frequency limit, there is weak Rayleigh scattering that decreases quickly with particle size, while in the optical limit of large f_{rel} the scattering cross section is close to 1. By increasing λ we decrease relative frequency (f_{rel}) and thus move closer to the Rayleigh limit. This was one of the motivations for using THz radiation.

Spectroscopy in field environments using terahertz has been demonstrated in several applications, for instance the remote detection of chemicals in Gopalsami et al. [2008] or the remote detection of nuclear radiation in Gopalsami et al. [2009]. Currently the spectra of H_2O as well as that of CO in the region 300-500 GHz are well known and included in the HITRAN database. This spectral range contains a few strong H_2O lines and a few conveniently places CO lines, shown in figure 1.2.

The absorption at the line centers is dependent on both concentration and temperature as shown in figures 1.3 and 1.4. Thus it is possible to determine these two parameters from measured spectra.

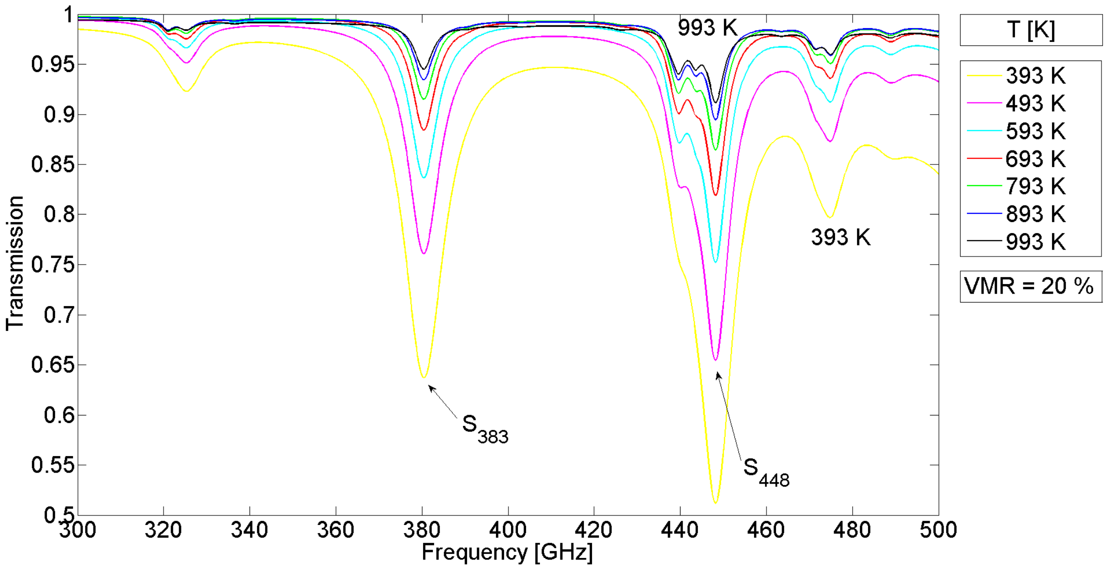

Figure 1.3: The simulated spectra of H_2O at $VMR = 20\%$ and varying temperatures. [data/AppendixC]

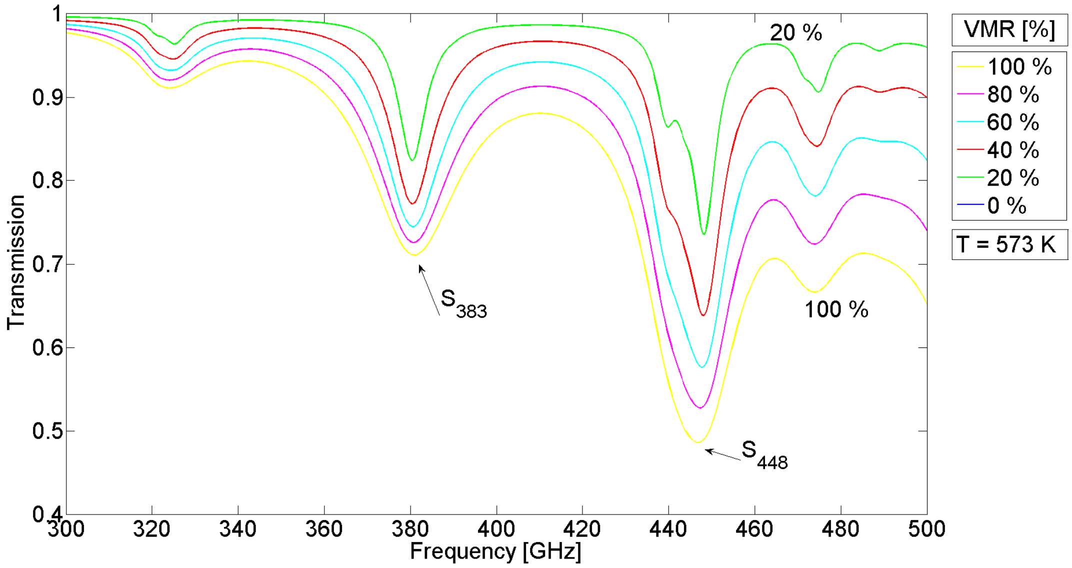

Figure 1.4: The simulated spectra of H_2O at $T = 573K$ and varying humidity. [data/AppendixC]

1.1 Data

Some of the data and code used for obtaining the figures in the text has been put in the following Google Drive folder:
`https://drive.google.com/folderview?id=0B25vmzARFvvOdnlYNDBocEFQNGM`

2

Theory

2.1 Gasification of biomass

Production of combustible gas from biomass can be achieved using several processess, including biological and thermal. In the present project, we are concerned with thermal gasification of biomass, particularly from wood pellets. However, many types of high-grade biomass are required in other industries and the energy sector will have to settle for the leftovers. Thus it will be necessary to handle a highly variable input in a process. This is why online detection of the product is required, since the process must be continuosly tuned to the variable input.

In thermal gasification the solid biomass is broken down thermally in the presence of an oxidising agent, in this case H_2O. The main products are CO, CO_2, H_2, CH_4, tars and other hydrocarbons. The dry gases and the water contents expected in the rawgas of the Chalmers gasifier are given in table 2.1, and for the fluegas data are given in table 2.2. Primary tars are of the form $C_xH_yO_z$, but are themselves broken down into either new tars, H_2 or the product gases mentioned. The process requires a temperature above 600^oC. (Gomez-Barea and Leckner [2010]).

The H_2O content is of critical importance in regulating the rate of the process, since it is involved in most reactions breaking down the large molecules of the fuel into product gas. The contents of the gas must be very finely tuned for downstream processes to work, which requires a low-delay monitoring of the most significant species. The intended downstream process in this case is generation of substitute natural gas (SNG), by the process of water gas shift:

$$3H_2 + CO \rightarrow CH_4 + H_2O \tag{2.1}$$

This is highly sensitive to the ratio of CO to H_2.

Table 2.1: The expected contents of gasifier rawgas at Chalmers power center, based on gas chromatography and H_2O separation by condensation. All VMR entries except H_2O refer to dry gas composition. (Hosein Bidgoli, private communication)

Gas	H_2	CO	CO_2	CH_4	C_2H_2	C_2H_4
VMR [%]	4.64	23.40	35.50	16.35	13.78	0.33

Gas (cont.)	C_2H_6	C_3H_6	C_3H_8	He	N_2	H_2O
VMR [%]	0.70	0.47	0.02	1.11	3.42	ca 65

Table 2.2: The expected contents of gasifier fluegas at Chalmers power center, based on gas chromatography and H_2O separation by condensation. All VMR entries except H_2O refer to dry gas composition. (Hosein Bidgoli, private communication)

Gas	N_2	O_2	CO_2	H_2O
VMR [%]	79.5	3.5	17	ca 20

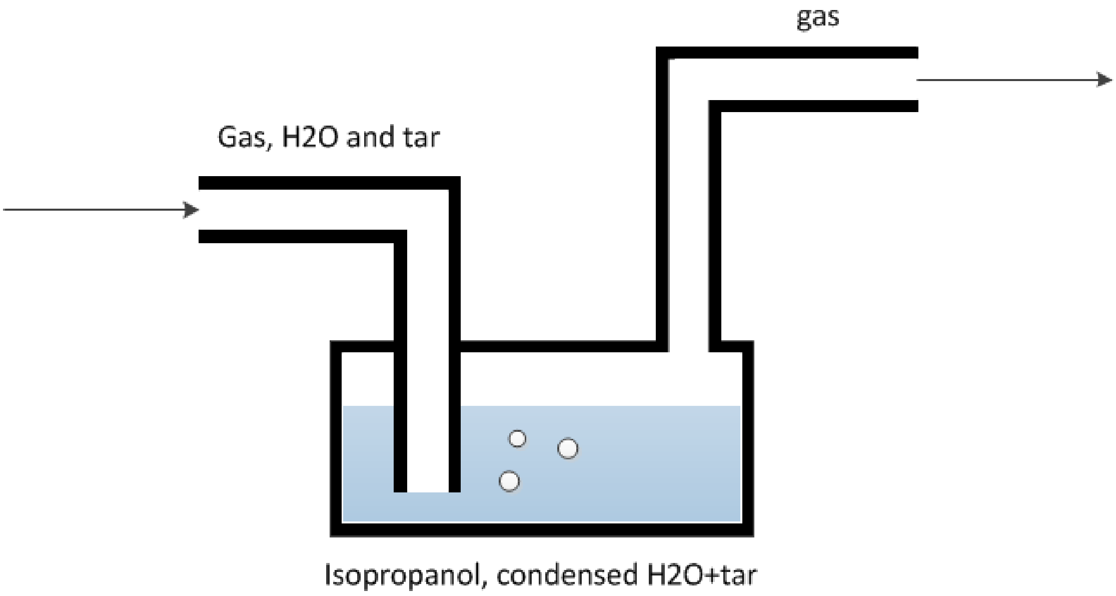

Figure 2.1: The device measuring H_2O content by condensation. H_2O and tar condense while bubbling up from the bottom of the isopropanol pool, and mix with the liquid. The mass increase of the isopropanol container gives the amount of H_2O and tar in a volume of gas, $\Delta m = m_{H_2O} + m_{\text{tar}}$. To give a good accuracy, the mass increase must be measured over periods of several hours.

Other methods than THz spectroscopy to monitor H_2O are IR spectroscopy or condensation (explained in figure 2.1). IR spectroscopy has the problems of increased scattering by the particulates, due to the shorter wavelength of IR compared to terahertz. The absorption of water is also very high in the IR, creating a risk of saturation of such spectrometers. Condensation is more robust: just let the H_2O condense and compare its mass to the volume of gas it came from. But this creates a long delay and also fails to differentiate between H_2O and tar, since tar also condenses. This motivates the attempt to use THz instead.

A gasifier has a bed of material with high heat capacity to keep the fuel at an even temperature. There are several designs of these beds, in the Chalmers case it is a fluidized bed, made of sand that has properties resembling a fluid when under the conditions of the gasifiers operation. The fuel is mixed with the bed material. Heat is provided by a separate combustion chamber, this is called external heating to differentiate from the case where the gasifier itself provides heat. Bed material is continously circulated between combustion chamber and gasifier to provide heat. Bubbles of steam will move upward through the bed material, accumulating gasifier products along the way. At this stage the particulates in the gas are small, submicron size, so they will not affect the THz radiation much. The temperature of flue- and rawgas leaving the gasifier is anticipated to be around 850^o C, which is the operating temperature of the process, but it cools down to about 350^o C before reaching the gas cell, since it is transported in heating hoses with a capacity of maximum 350^o C. It is then heated again inside the oven to 430^o C to avoid condensation in the gas cell.

Figure 2.2 shows a flow diagram of the process at the Chalmers gasifier. Fuel is fed from above into both chambers. In the combustion chamber, air is injected for combustion while in the gasification chamber steam, the oxidizing agent, is inserted instead. Heat is transported from the combustion chamber to the gasification chamber by circulation of the hot sand of the fluidized bed. The output gas of the combustor is referred to as fluegas, while the product gas of the gasifier is called rawgas when it is leaving the gasifier, before being cleaned for downstream use.

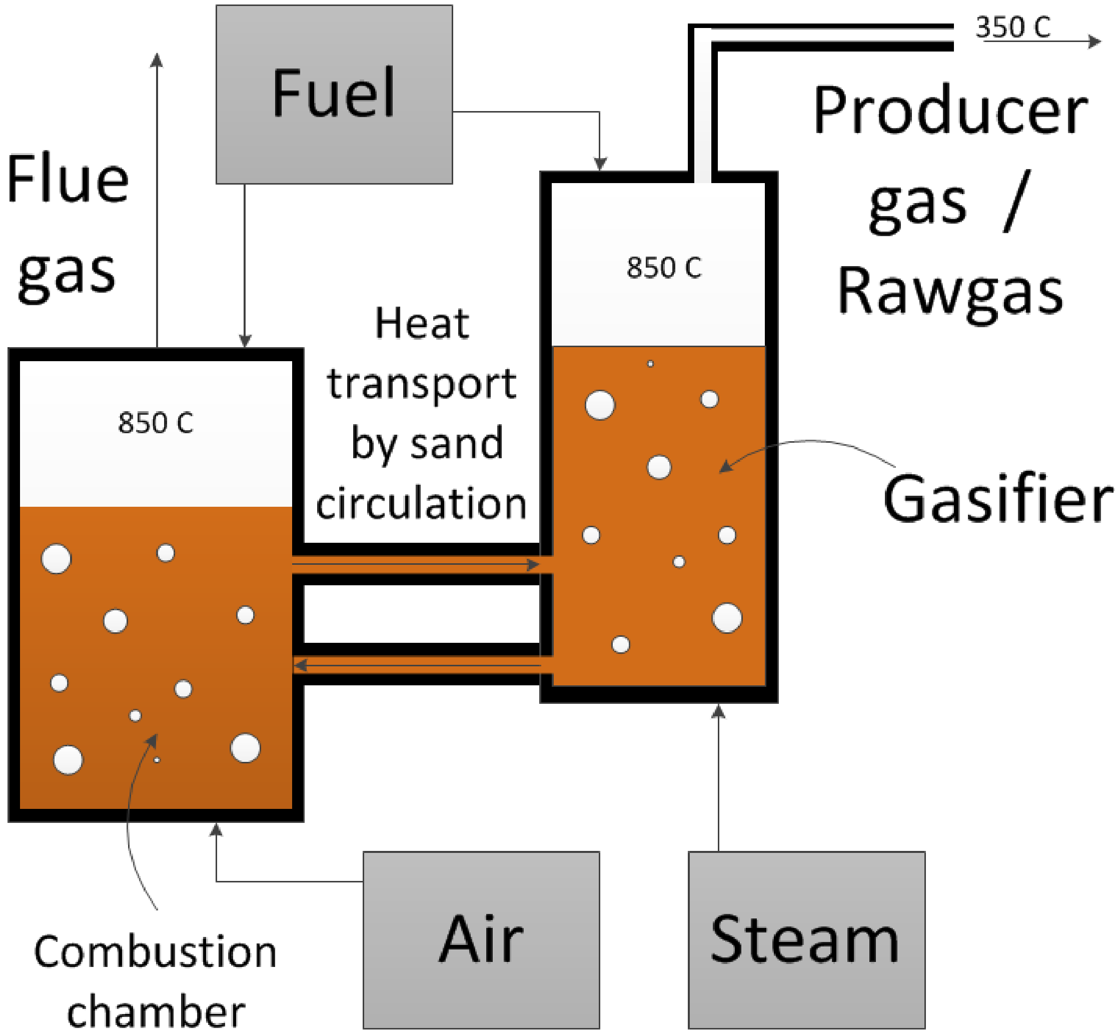

Figure 2.2: The operating principle of the Chalmers gasifier

2.2 Terahertz technology

The terahertz region of the electromagnetic spectrum is defined as wavelengths from 3mm to 30 μm. It starts at the upper edge of millimeter waves and ends at the lower edge of the infrared. Generation and detection of radiation in this range is more difficult than in the microwave region of the EM spectrum, and THz equipment is currently an area of intense research.

Several applications of THz radiation exploit its ability to penetrate tissue, fabric and plastics to a significant depth, while being partially reflected depending on density and contents of objects. This makes possible a variety of imaging applications. In addition, it is non-ionizing[1] and thus harmless to living organisms unless used with very high power output, which tends to be neither needed nor available. In the present project, we attempted to exploit THz radiation in the monitoring of water vapor content in dirty gasifier rawgas, where IR laser spectroscopy fails due to the particulate matter in the gas. THz was expected to pass through the particulates. We also face the issue of high temperatures. Temperature affects spectral lines both by changing their relative strengths and by broadening of lines. This is further described in section 2.3.2.

2.2.1 H_2O and CO absorption at Terahertz frequencies

We need to detect H_2O under various concentrations and temperatures. It is important to avoid saturation of the spectrometer. In figure 2.3 we show the spectra of H_2O as well as CO. Three of the H_2O lines are very strong and risk to saturate our system. We want several weak lines in the frequency range used. The band 300-500 GHz suits this purpose for both gases considered, and equipment for sweeping over these frequencies exists. The danger of saturation is exacerbated by high temperatures, which increase absorption significantly. See appendix C for plots of the temperature dependence of absorption at various concentrations of H_2O.

---

[1] Photon energies vary from 0.413 meV at 3 mm to 41.3 meV av 30 μm

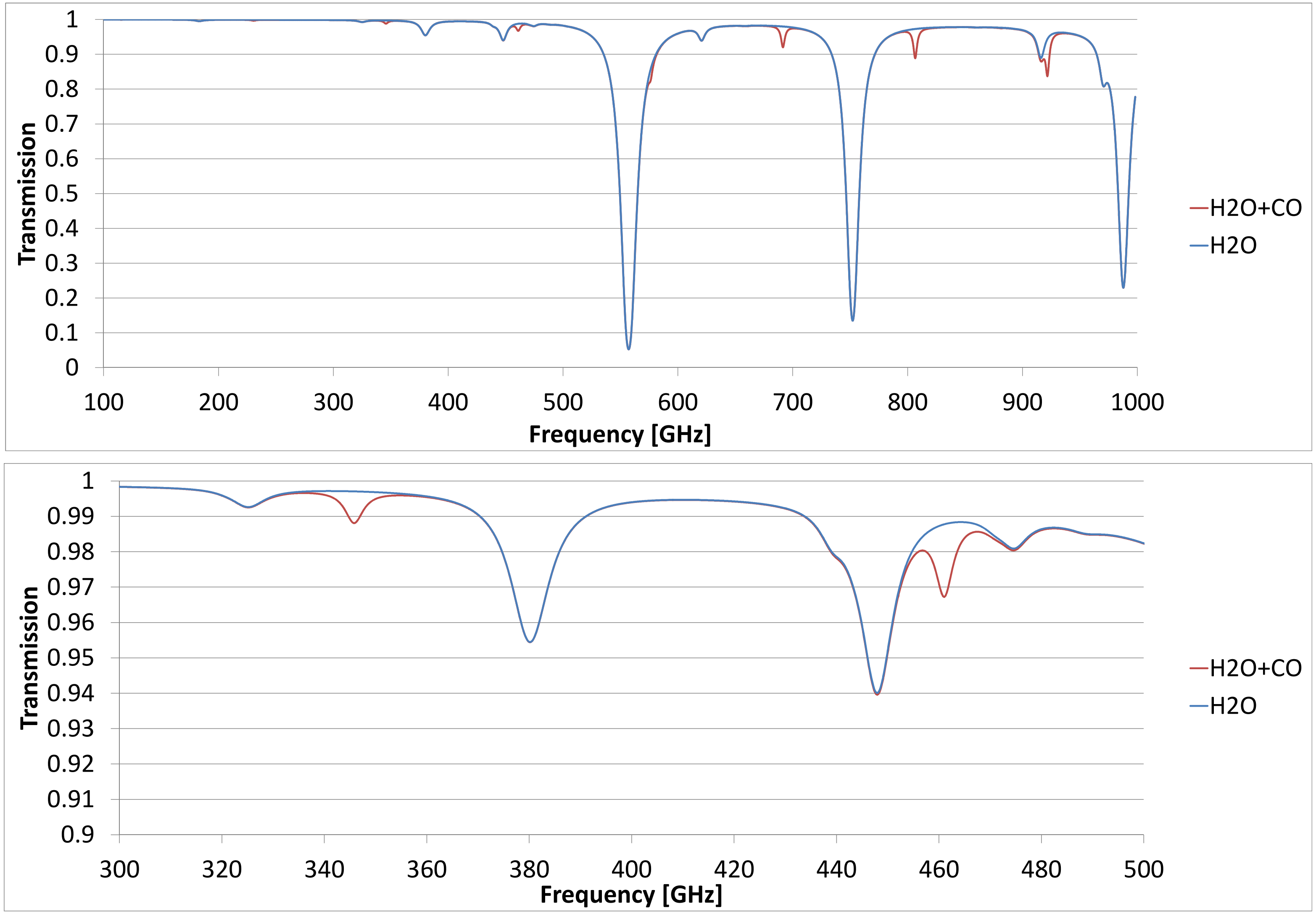

Figure 2.3: Top: Spectra of 10% H_2O and 10% CO + 10% H_2O in the range 100GHz to 1 THz at 296 K. Bottom: The same restricted to 300-500 GHz. [data/simulation full]

2.2.2 Detectors and sources

Detectors for THz can be broadly categorized into thermal or photon detectors, as Rogalski and Sizov [2011] describe. Thermal detectors absorb the radiation and gain heat, which induces change in some physical property of the material that can be easily measured. For instance, metals or semiconductors can be used that change their electrical conductivity in response to temperature differences. This is a common category of detectors called Bolometers. Another example would be to measure the thermal expansion of a gas, which is the method we use. That type of detector is called a Golay cell and is described in detail in section 3.2.2. Thermocouples are devices that generate voltage over a junction of two different materials in response to temperature changes. They are used in many applications and can be used as IR detectors as well as for temperature measurements in general.

Photon detectors rely on excitations in semiconductors. When a photon is absorbed its energy gives rise to an electron-hole pair. These gives rise to electrical conduction, in a variety of ways for different detector types. They have a frequency-dependent response, unlike thermal detectors. Their advantage is that they tend to have very fast response times and good signal-to-noise ratio. A major inconvenience is that they require cooling to very low temperatures to avoid thermally generated noise. A thermal detector is for this reason the favoured option provided that its precision is acceptable. The Golay cell was used because it was available. We list some detector types in table 2.3. A measure of detector sensitivity in common use is Noise Equivalent Power, NEP. It is defined as the power required of an input signal to generate a signal-to-noise ratio of 1 in an output signal with 1 Hz bandwidth. The unit is $\mathrm{W}\ /\sqrt{\mathrm{Hz}}$. This should of course be as low as possible for good detectors. A few examples from Rogalski and Sizov [2011] are collected in table 2.4. A higher sensitivty of a detector lessens the noise and shortens the required integration time at a particular noise level.

Table 2.3: Detector types for far IR and THz. A summary of Rogalski and Sizov [2011]

Category	Detector type	Mechanism
Thermal	Bolometers	Temperature dependence of conductivity
	Thermocouple	Voltage generated by temperature change
	Pyroelectric	Charged plane conductors changing polarity
	Golay cell	Thermal expansion of gas
Photon	Photoconductors	Photon absorption in energies above the band gap creates carrier/hole pair in a uniform piece of some semiconductor, raising conductivity.
	p-n junction diodes	Photon-induced pair production creates a photocurrent across a junction between p- and n-doped semiconductors
	Schottky barrier diodes	Photocurrent across Schottky barrier

Table 2.4: Sensitivity for some detector types for far IR and THz. A summary of Rogalski and Sizov [2011], last entry is a bolometer made at TML, MC2, Chalmers. Described in Cherednichenko et al. [2011].

Detector type	NEP [W /$\sqrt{\text{Hz}}$]
Golay cell	$10^{-9} - 10^{-10}$
Schottky diode	10^{-10}, increasing with ν
Bi bolometer	1.6×10^{-10}, increasing with ν
Nb microbolometer	5×10^{-11}
Ti microbolometer	4×10^{-11}
Ni microbolometer	1.9×10^{-11}
YBCO bolometer	3.7×10^{-10}

2.2.3 Waveguides

Waveguides are conducting tubes used to transfer radiation with as little attenuation as possible. Their dimensions are chosen with respect to the wavelength of the radiation considered, and longer wavelengths require broader waveguides. Each waveguide geometry has a cutoff frequency below which decay of the transmitted wave will occur. All waveguides that are not perfect conductors will experience attenuation, which is lower for higher frequencies. The minimum attenuation naturally occurs for an infinitely large waveguide, but detector apertures tend to be quite small and one needs to balance these two requirements. Conical horns at the end of the waveguide is one way of balancing these needs. Waveguides at which the intended wavelength is small enough to allow ”overmoding”, where many additional modes of propagation can occur, are called oversized waveguides. These give a low attenuation, but less mode purity. Such a waveguide was used in this project. It is oversized since it has an internal diameter of 26 mm while the longest wavelength used is 1 mm. In our case only the total transmitted energy is measured, the Golay cell treats all modes of propagation equally, so overmoding is not a big problem.

2.3 Molecular spectroscopy

When EM radiation passes through a sample, its rate of transmission will depend on various properties of the sample. The Beer-Lambert law formulates this as:

$$T = T_0 e^{-Al} \tag{2.2}$$

where l is the length of the sample along the beam and A is an absorption coefficient, depending of a number of parameters. Since these parameters are specific to the substances in a sample, as well as to some other conditions such as pressure and temperature, one can infer facts about the sample by studying its absorption spectrum. Calculating the absorption in relation to the pressure, temperature and composition is the subject of the following sections.

2.3.1 Energy levels

In an atom there are only electronic energy levels, which usually have optical transitions. Some fine structure transitions are in the terahertz, though. When forming a molecule, valence electrons of the constituent atoms will inhabit molecular orbitals instead of the atomic orbitals, with somewhat different energies. But there are also new degrees of freedom present. Molecules do not have rotational symmetry and will thus have rotational energy. The rotation must be treated quantum mechanically by rewriting the expression for rotational energy with quantum mechanical operators, and this gives rise to quantized rotational states. This will be demonstrated for CO below. Each molecular bond will in addition introduce vibrational modes, giving a spectrum of vibrational states. The number of vibrational modes depends on the molecule. A diatomic molecule such as CO has only one vibrational mode, while water is more complicated and has three vibrational modes. A sketch of the various modes of the two molecules is given in figure 2.4.

To calculate electronic energy levels in molecules one uses the Born-Oppenheimer approximation: nuclear and electronic motion are assumed to be completely separate. This is justified since electron mass is about two thousandths of the mass of a nucleon, thus moving much quicker. In effect, electron wavefunctions depend only on the position of the nuclei and the motion of the nuclei depends only on the time-averaged distribution of electrons. Another approximation that might be used is to consider the molecule a rigid rotor when calculating rotational energy levels. Without this assumption there is some vibration-rotation coupling. This is however true to a significant degree at higher energy levels and then the rigid rotor approximation has to be abandoned. Vibration can be modeled as a harmonic oscillator for low energy levels, but at high energy levels it must be replaced by an anharmonic oscillator that couples to the rotation.

While rotation-vibration in diatomic molecules can be handled analytically with ease the difficulty increases enormously for even triatomic molecules such as water. Theses are written on this subject, for instance Lori [2008]. A basic description of the vibrational levels would be a linear superposition of single-mode vibrations, but calculating exact levels requires handling nonlinear effects. We instead describe the diatomic molecule.

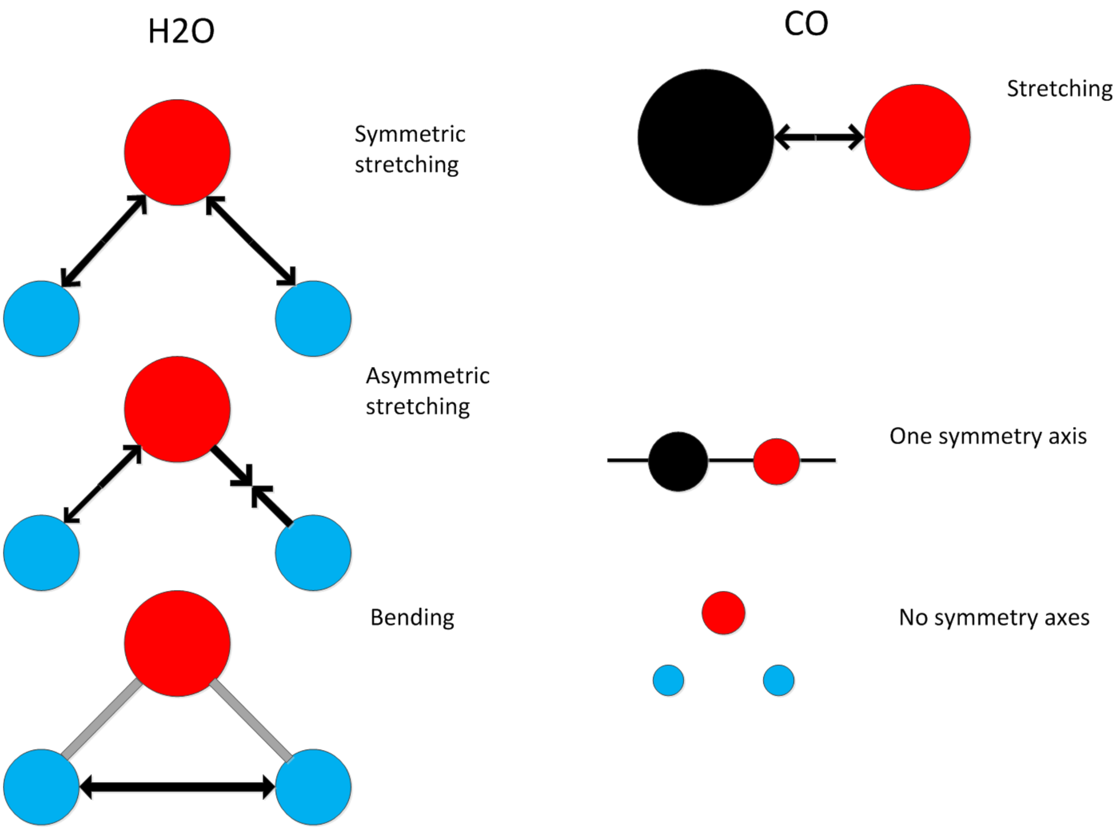

Figure 2.4: vibrational modes and rotational axes of CO and H_2O

The vibration-rotation spectrum of CO

Vibration of CO is modeled as a harmonic oscillator for low energy levels (McQuarrie [2008], chapter 5), so the energy levels are of the form $E_{\text{vib}} = (\nu + \frac{1}{2})\hbar\omega$ where $\omega = \sqrt{\frac{k}{\mu}}$ is determined empirically. μ is the reduced mass and k is the bond force constant. These lines generally are in the infrared. For CO, $\nu = 1 \rightarrow 2$ is at 269 meV or 65 THz.

Rotation of CO is modeled as a rigid rotor with length r_e, the interatomic distance at equilibrium. Its moment of inertia, with respect to a line normal to the bond and intersecting it at the center of mass, is then given by $I = \mu r_e^2$ where μ is the reduced mass of the two-body system. We can insert this in the Schrödinger equation expressed in terms of the angular momentum operator J:

$$\frac{J^2}{2I}\psi = E_{\text{rot}}\psi \tag{2.3}$$

with eigenvalues $E_{\text{rot}} = \frac{\hbar^2}{2I}j(j+1)$. In the case of CO we do not have to worry about the other rotational axes, one is identical and the other is a symmetry axis. Inserting the parameters for CO (from Hush and Williams [1974]) gives $E_{\text{rot}} = 0.24j(j+1)meV$. This

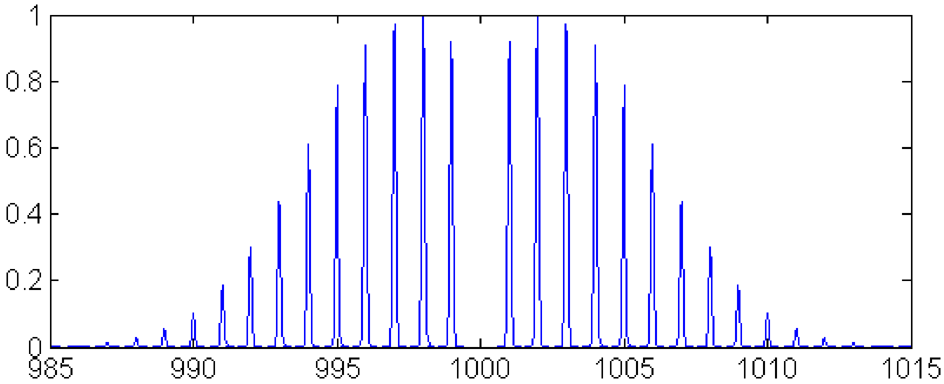

Figure 2.5: Sketch of typical rovibrational spectrum for a diatomic molecule with a vibrational transition at 1000, and rotational constant of 1/2, in arbitrary units.

is a multiple of about 58 GHz, starting in the microwave region. It is not surprising that rotational lines are also present in the neighboring THz region. The energy of the transitions has a clear hierarchy, electronic>vibrational>rotational. Rotiational transitions are on the order of 1-10 cm^{-1} compared to about 1000 cm^{-1} for vibrational transitions. For each vibrational level one can thus superimpose rotational transitions and get a spectrum such as that sketched in figure 2.5. Selection rule $\Delta J \neq 0$ suppresses the pure vibrational transition, which is surrounded by two branches of rotational transitions, the lower energy P-branch for $\Delta J = -1$ transitions and the higher energy R-branch of $\Delta J = 1$.

Similar principles apply for the water molecule, but the calculations are very involved. Both CO and H_2O have rotational lines in the region 300-500 GHz, where we have measured. See figure 3.15 for the rotational lines of CO. They can be easily understood, while the H_2O lines in figure 3.14 are more complex. In practical applications one uses semiempirical rather than calculated spectra.

2.3.2 Line shape

The line shape is affected by pressure- and temperature induced broadening, temperature dependences in line strength, and line mixing. There are three main types of line broadening (Liou [2002], chapter 1):

- Natural broadening: due to the time-energy uncertainty principle.
- Doppler broadening: due to doppler shifts of the radiation from sources moving in all directions.
- Pressure broadening: due to several pressure-dependent effects including collisions (shortening excited state lifetimes) and perturbations of the energy levels of atoms by the electric fields of nearby atoms.

We briefly describe these types to show which are important in our case.

Natural broadening

This type of broadening is the most fundamental, existing due to the Heisenberg uncertainty principle:

$$\Delta E \Delta t \geq h/2\pi \tag{2.4}$$

The lifetime of a state is thus inversely proportional to its uncertainty in energy. Unless states in the gas are extremely short-lived, this is completely negligible.

Doppler broadening

The velocity of molecules in a gas follow a Maxwell distribution:

$$p(v) = \frac{1}{\sqrt{\pi} v_0} e^{v^2/v_0} \tag{2.5}$$

where v_0 is the mean speed given by $v_0 = \sqrt{2k_B T/m}$. This gives rise to a Gaussian lineshape:

$$f_D(\nu - \nu_0) = \frac{1}{\alpha_D \sqrt{\pi}} exp\Big(- \frac{(\nu - \nu_0)^2}{\alpha_D^2} \Big) \tag{2.6}$$

where $\alpha_D = \nu_0 \sqrt{\frac{2k_B T}{mc^2}}$. This type of broadening is significant at very high temperatures or at low pressures, and the temperatures in our case might be high enough.

Collisional broadening

Collisional broadening follows a Lorentz line shape:

$$f(\nu - \nu_0) = \frac{\alpha/\pi}{(\nu - \nu_0)^2 + \alpha^2} \tag{2.7}$$

where

$$\alpha = \alpha_0 \Big(\frac{p}{p_0} \Big) \Big(\frac{T_0}{T} \Big)^n \tag{2.8}$$

Where α_0 is the halfwidth at reference temperature T_0. The half-width is composed of the self- and foreign-broadened halfwidths, that are added with weighting in accordance with the volume mixing ratio (VMR) of the gases present. This type of broadening is very significant in atmospheric pressures and temperatures, and in the temperature range we are to operate in.

Combined broadening

If more than one type of broadening is relevant the lineshape functions can be convoluted to get a realistic shape. When convoluting the Lorentz and Gaussian functions, one gets the Voigt function, a function for which there is no closed form expression. This could possibly improve our modelling algorithm.

Temperature dependence of line strength

The line strength parameter $S_i(T)$ is necessary to determine the shape of the spectrum. It has a temperature dependence given by:

$$S(T) = S(T_0)\frac{e^{-hcE_L/k_BT}Q_T(T_0)[1 - e^{-hc\nu_0/k_BT}]}{e^{-hcE_L/k_BT_0}Q_T(T)[1 - e^{-hc\nu_0/k_BT_0}]} \tag{2.9}$$

where T_0 is a reference temperature and T is the temperature considered. Q_T is the thermodynamic partition function and is specific to each chemical species. E_L is the energy of the lower state in the transition and ν_0 is the frequency of the line center.

Line-by-line models

To calculate the transmission profile one must sum the contribution of all nearby lines, one at a time. We describe how to do this in the most straightforward way, although highly optimized schemes exist for saving computational power. The direct approach is to calculate the contribution of each spectral line at each frequency and sum over all spectral lines in the vicinity of the spectral range of interest. The transmission at frequency ν can be written as

$$T(\nu) = \sum_i \Big[S_i(T)f(\nu - \nu_i; \alpha_i)l\Big] \tag{2.10}$$

there T is total transmission, S_i is line strength of line i, f is a shape function (Lorentz under atmospheric and similar condition), α is the Lorentz half-width and l is the length of the radiations passage through the medium. The α is itself affected by pressure, temperature and VMR of gases as described above.

2.3.3 Collisional line mixing

An effect that is significant in IR gas spectroscopy is pressure-induced collisional mixing of lines. Adjacent lines will interfere with each other to a significant degree, which will create line profiles the differ significantly from the ones calculated by a line-by-line Lorentz-profile model. To see why this is so, we refer to a toy example by Hartmann et al. [2008], chapter four, pp. 148. The example assumes we have a pair of transitions $i \rightarrow f$ and $i' \rightarrow f'$, both in the optical range. If the transitions $i \rightarrow i'$ or $f \rightarrow f'$ are very small, they might be triggered by collision, thus introducing processes such as $i \rightarrow i' \rightarrow f'$ that mix the two optical lines. An illustration is shown in figure 2.6. While we obviously don't get mixing between optical states of different molecules, the lineshapes of a molecule will still be affected by molecules of other species as well as its own kind. This is due to the low energy transitions triggered in the collisions, that transfer energy from one molecule to another in a way that is specific for each pair of molecules. To calculate the effects of line mixing one thus needs calculated or empirical mixing coefficients for each combination of gases. There is a large number of models for handling line mixing with varying precision and computational complexity, from simple classical models to full quantum scattering models.

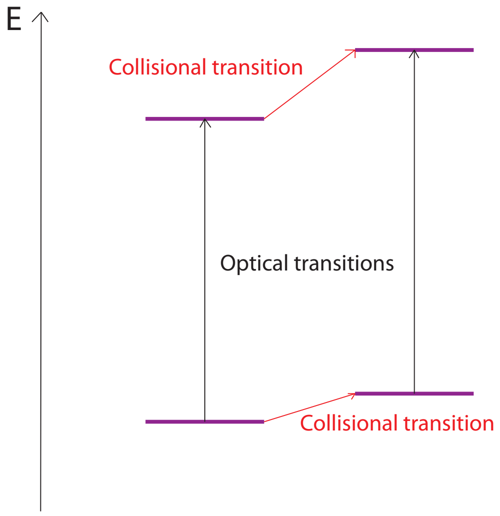

Figure 2.6: The type of transitions giving rise to line mixing.

2.3.4 The HITRAN database

The HITRAN (high-resolution transmission molecular absorption) database contains empirical data on a large number of spectral lines for a number of molecules, including CO and H_2O. It contains intensities and positions as well as lineshape parameters over a wide range of frequencies. The foreign-broadened halfwidths are given with respect to air. The database contents as of 2008 are described by Rothman et al. [2009].

2.3.5 LINEPAK vs custom algorithm

Since the effects described above are quite complex to simulate, much work has been done by researchers on optimizing algorithms for this task. In this project we used the webservice SpectralCalc, provided by GATS, Inc and powered by the LINEPAK library of GATS founder L. Gordley, described in Gordley et al. [1994]. The simulation takes all of the effects mentioned above into account and automatically collects needed data from HITRAN. It proved less tedious to extrapolate from a dataset obtained using SpectralCalc rather than perfecting a custom algorithm for spectral simulation. The primary difficulty in simulating spectra in the range considered in this project is the complexity of line mixing, which is very significant for H_2O. The line-by-line Lorentz-profile algorithm is included in appendix A. The dataset downloaded from Spectralcalc.com is described in appendix C.

3

The setup

3.1 Gas cell design

The gas cell was a sealed steel tube (with inner diamter 26 mm and outer diameter 33 mm) with dual windows at both ends. The compartment for the sample gas was 1 m long, and in total the tube was 1.8 m long. The inner windows were made of crystalline quartz, 5mm thick, and the outer ones were made of teflon, 2mm thick. Both window materials are mostly transparent in the frequency range used, the transmission as function of frequency is plotted in figure 3.6. The windows where inserted at a 60^o angle to the beam to minimize standing waves and other unwanted reflections. The gas cell was fully enclosed, except for the ends, by an oven (Entech ESTF 50/11-11) to keep the temperature stable. A sketch of the cell is shown in figure 3.1 and its connections to the other system components is shown in figure 3.2. A photo of the gas cell is shown in figure 3.5.

In the laboratory setting, nitrogen gas was injected at a rate of 5L/min using a Bronkhorst EL-FLOW mass flow controller, and pre-heated using heating hoses from Hillesheim, model H3406-030-08-250C-83 and temperature controllers HT-40. Steam was injected into the nitrogen stream before entering the gas cell, using a steam generator from Cellkraft (E-1000 precision evaporator). The gas flowed continuously through the gas cell and exited at the opposite end into the open air. Thus a temperature gradient formed when equilibrium was reached, and this was approximately measured with thermocouples at inlet and outlet. Figure 3.4 shows a photo of the setup. The volume between the windows was continously flushed with N_2, with mass flow controllers set to 1 L/min, to avoid contamination with H_2O or other gases.

In the gasifier setting, the input rawgas came directly from the gasifier, and exited into the gas cleaning apparatus of the facility. Fluegas was also measured, directly from the combustor. Several times the input gas was also switched to bottle gas for testing of CO detection. Figure 3.3 shows a photo of the setup.

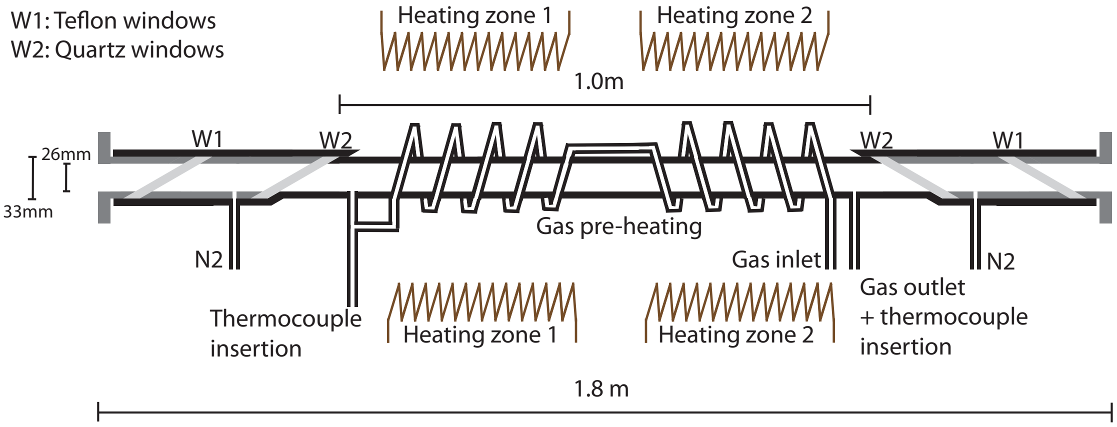

Figure 3.1: A sketch of the gas cell

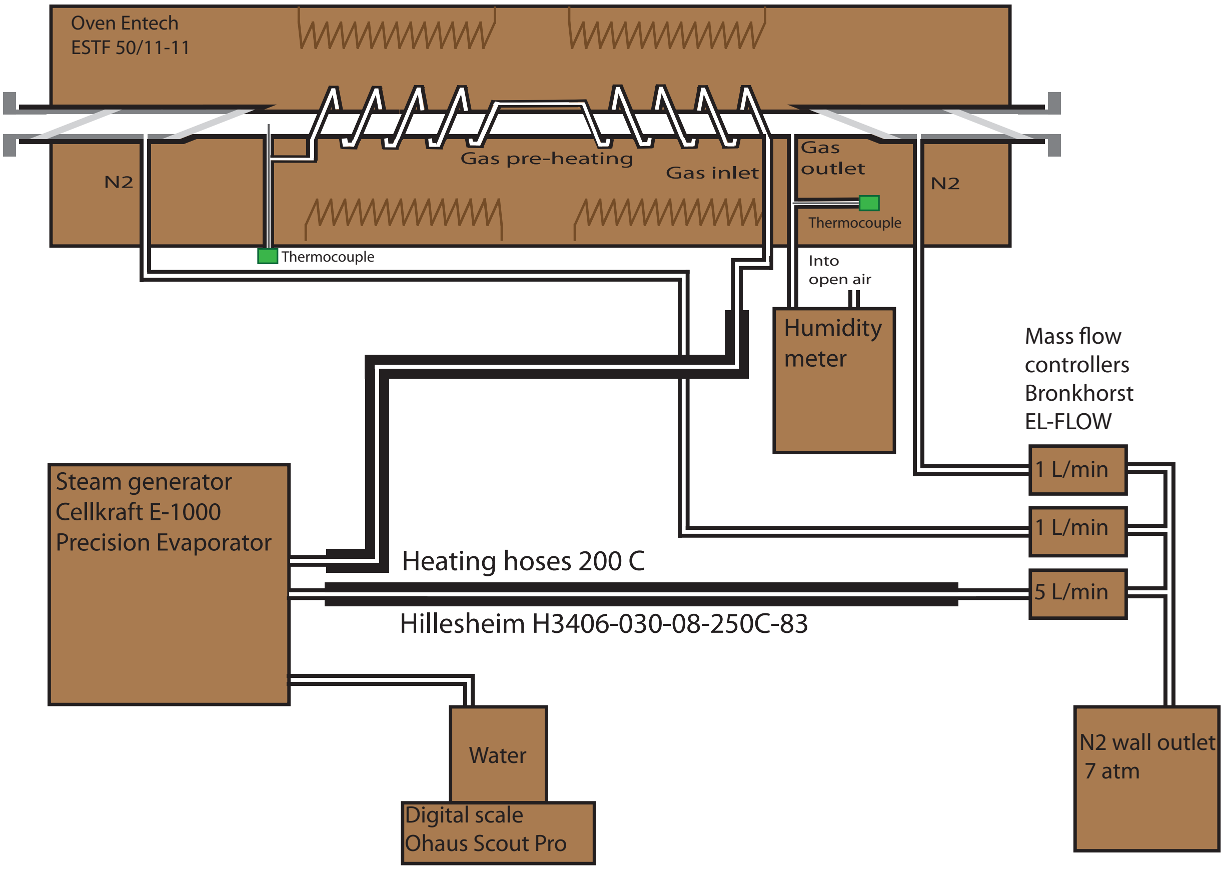

Figure 3.2: The gas cell and its connections to the rest of the system.

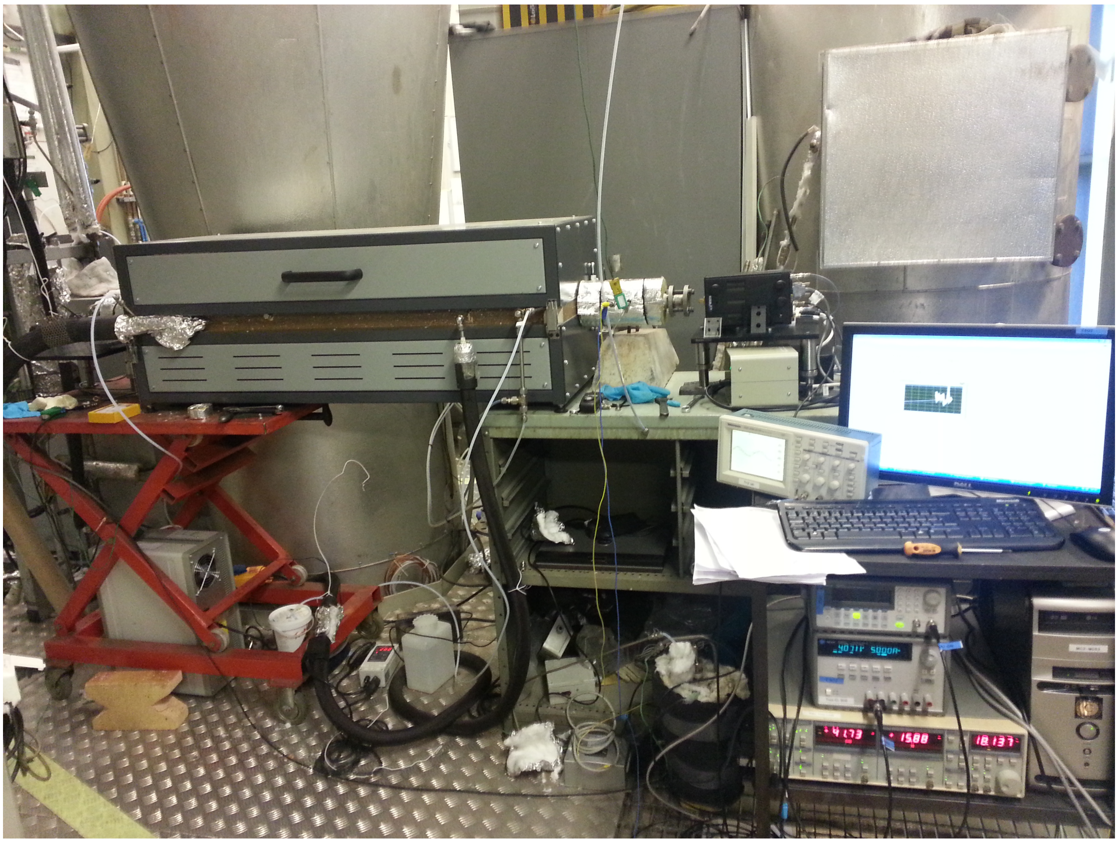

Figure 3.3: The gas cell set up at the gasifier

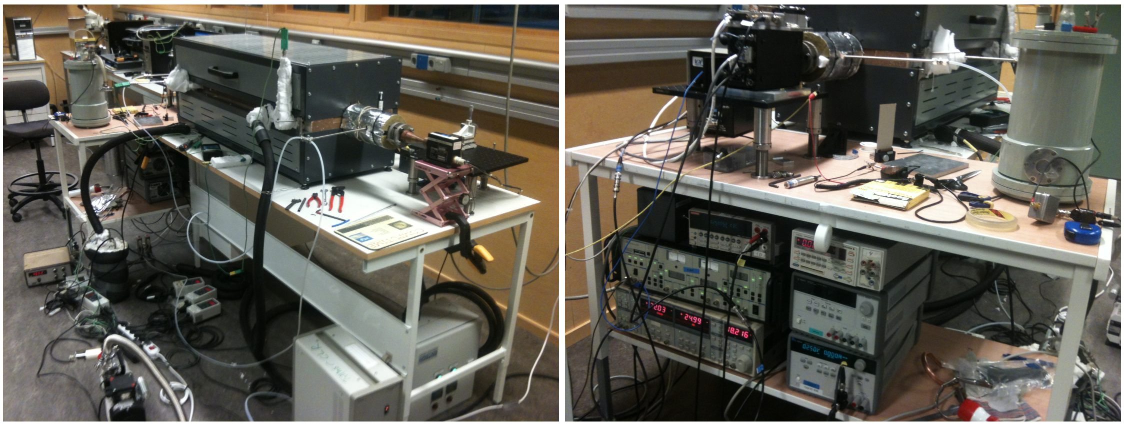

Figure 3.4: The gas cell in the lab within the closed oven, tubing and electronics.

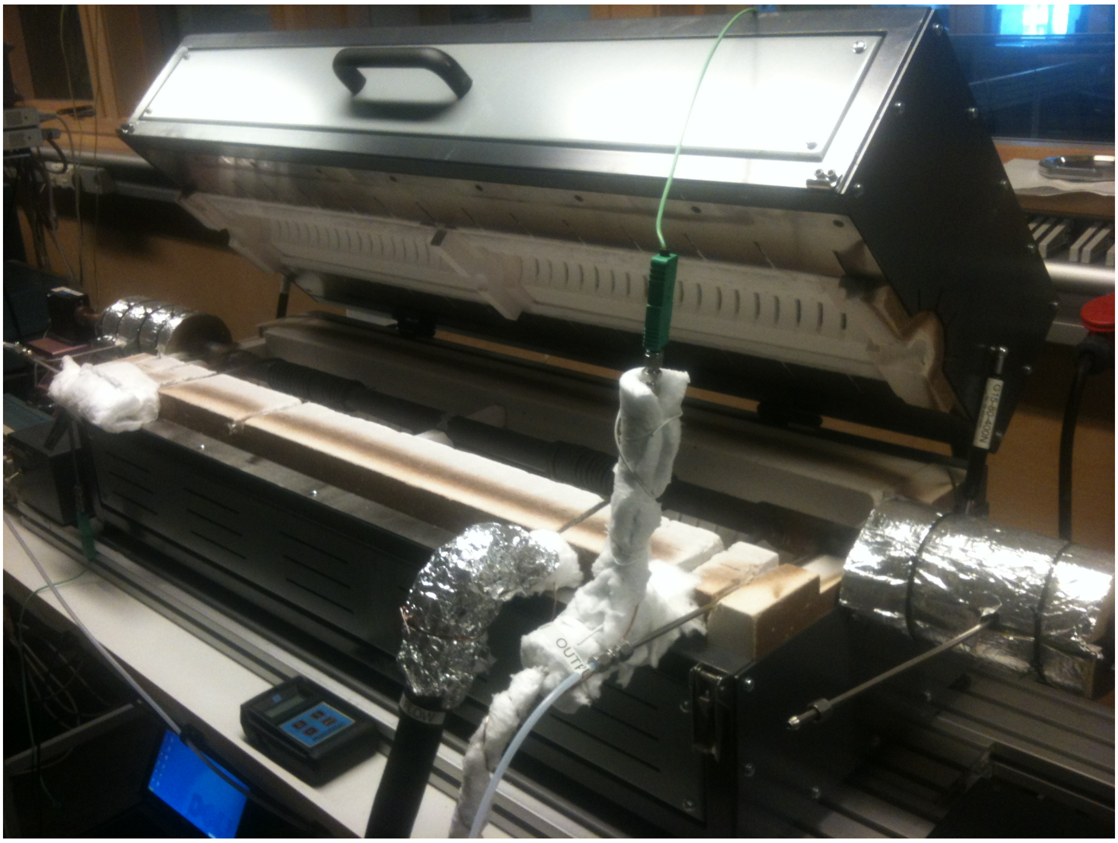

Figure 3.5: The gas cell inside the open oven

3.1.1 Window properties

The transmission through the windows of the gas cell was measured. The two window types were quartz (5 mm) and teflon (2 mm), and their transmissivity as function of frequency is given in figure 3.6. The refractive index is obtained by the equation (Hecht [2001], chapter 9.6).

$$\frac{\lambda}{n} = \frac{2L}{m} \tag{3.1}$$

where m is the number of standing wave nodes between the window surfaces and has to be an integer. When it is, we will have a peak in the transmission due to a standing wave. We could set $m = 1$ and let $\nu = c/\lambda$ be the frequency difference between two of our observed peaks in the transmission. Then

$$\nu = \frac{c}{2Ln} \tag{3.2}$$

in our cases we can se in figure 3.6 that ν is 16 GHz for quartz, corresponding to $n = 1.88$ and for teflon ν is about 7 GHz corresponding to $n = 1.43$.

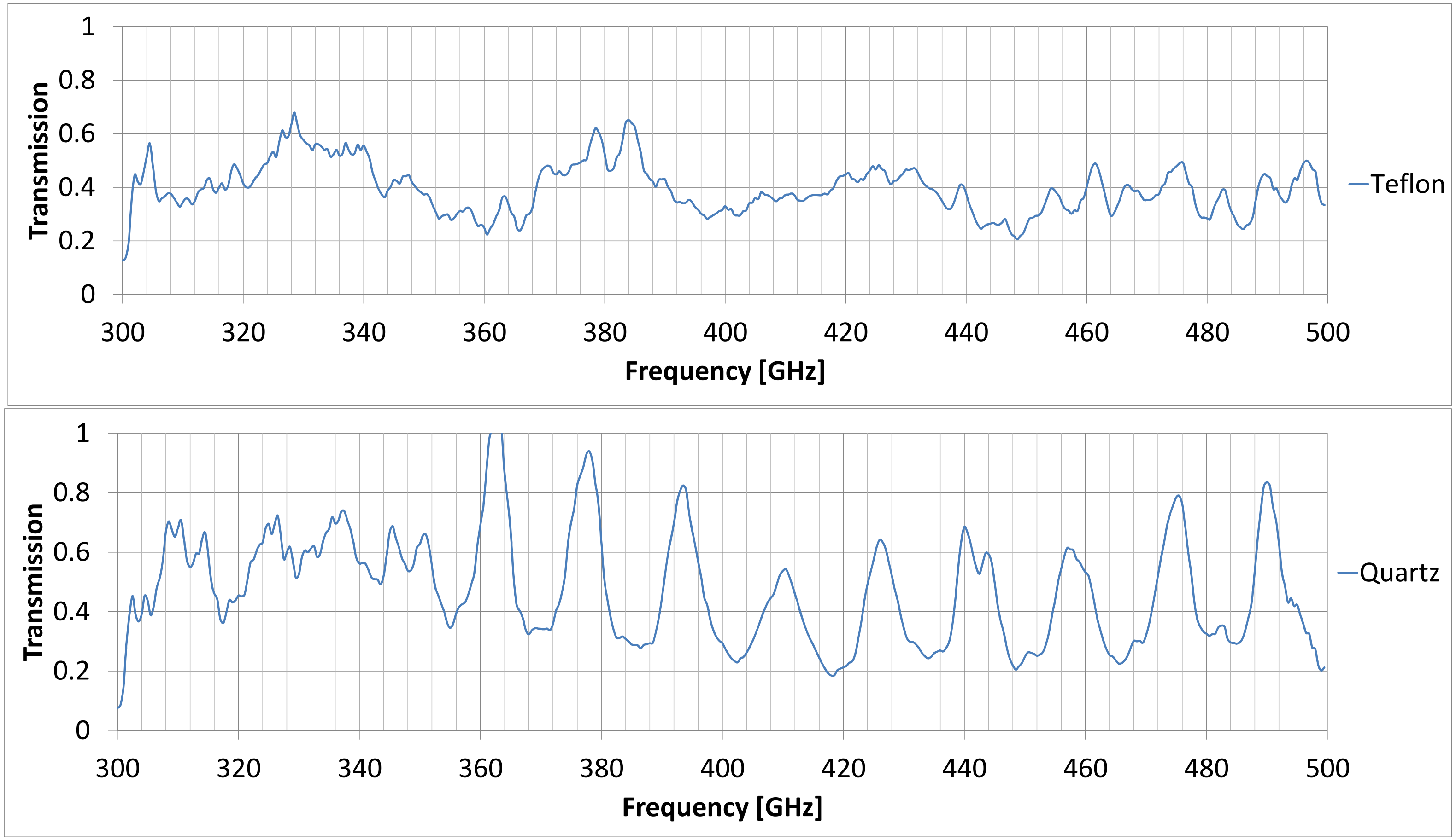

Figure 3.6: Transmission through teflon(top) and quartz(bottom) windows at normal incidence relative to air. [data/windowproperties/]

3.2 Spectrometer

The spectrometer setup consisted of a source, a detector and a reference detector as shown in figure 3.7. All instruments were controlled from a PC with LabVIEW using GPIB (IEEE 488).

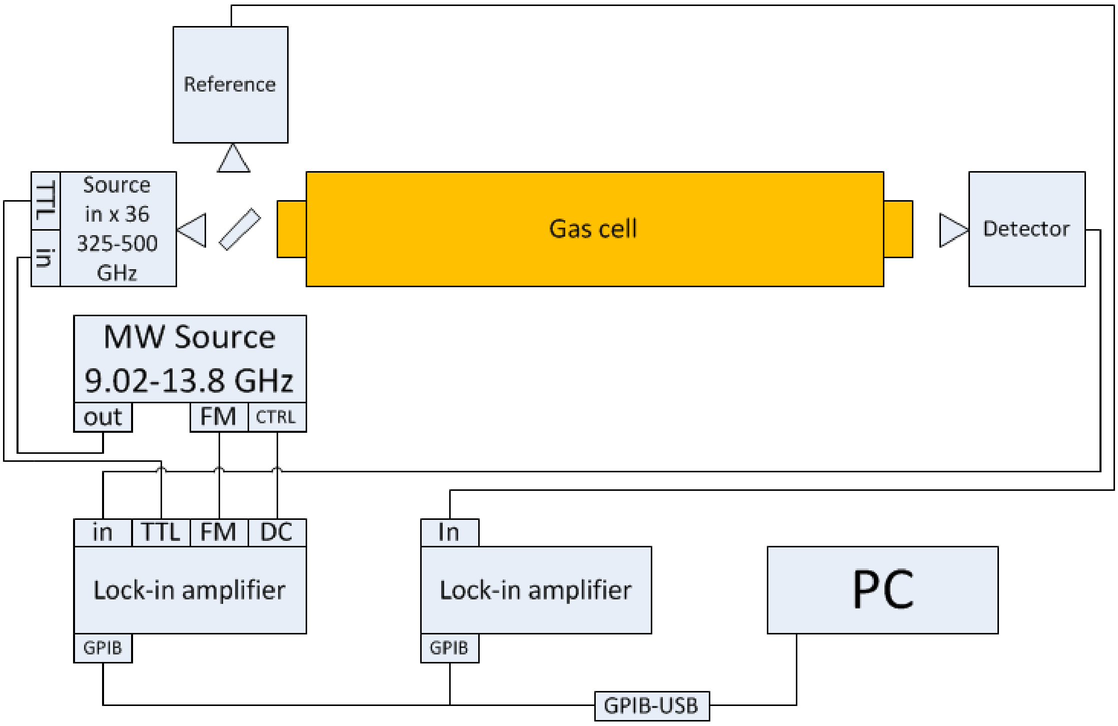

Figure 3.7: The setup of the instruments around the gas cell

3.2.1 Source

Since we required a tunable source in the range 300-500 GHz, we used first a tunable microwave source over a lower frequency range, then an amplifier/multiplier chain (AMC) multiplying the frequency in several steps up to the THz range. A block diagram of the devices is shown in figure 3.9. The microwave source was a Virginia Diodes Tx 195, driving a Virginia Diodes WR2.2AMC with input frequency range 9.0-13.9 GHz and output frequency range 325-500 GHz. The source is shown in figure 3.12 and the AMC in figure 3.13. We used the TTL output on the lock-in amplifier for amplitude modulation of the source, set to a frequency of 18 Hz. The frequency of the output signal from of the microwave source was controlled by a DC control voltage, for which we used the auxiliary outputs of the lock-in amplifier. The detected signal, an 18 Hz AC voltage, was then read out using the same lock-in amplifier. The correspondence between DC control voltage U_{ctrl} and output frequency f_{out} [GHz] was given by

$$U_{\text{ctrl}} = (f_{\text{out}}/36 - 8.0074)/1.1998 \qquad (3.3)$$

Where the upper limit on U_{ctrl} was 5 V. Since there is a large power variation in the frequency setting(see figure 3.8), we used frequency modulation to have some built-in signal averaging. FM was controlled by an AC output on the lock-in set to a frequency of 333 Hz. The amplitude of the FM control signal was set to 5 V which gave rise to a slightly nonlinear frequency swing in the final output signal, given for two different control voltages in table 3.1. The output power of the source specified by VDI is shown in figure 3.10.

Table 3.1: Amplitudes of frequency swings due to modulation with various amplitudes. Δf_{in} is the maximum deviation from the mean frequency at any particular value of the control voltage U_{ctrl}, and is due to the value of the FM voltage U_{FM}. Δf_{out} is the output frequency of the AMC after multiplication. The relation between FM modulation voltage and output frequency swing varies slightly across the operating range of our source, as can be seen in the difference in output from these two control voltages when all other parameters are kept constant.

U_{ctrl}[V]	U_{FM}[V]	Δf_{in}[V]	Δf_{out}[GHz]	U_{ctrl}[V]	U_{FM}[V]	Δf_{in}[V]	Δf_{out}[GHz]
2.2	1	0.004	0.144 4	4.8	1	0.005	0.18
	2	0.008	0.288		2	0.009	0.324
	3	0.012	0.432		3	0.013	0.468
	4	0.016	0.576		4	0.017	0.612
	5	0.02	0.72		5	0.021	0.756
	-1	-0.005	-0.18		-1	-0.004	-0.144
	-2	-0.008	-0.288		-2	-0.008	-0.288
	-5	-0.021	-0.756		-5	-0.021	-0.756

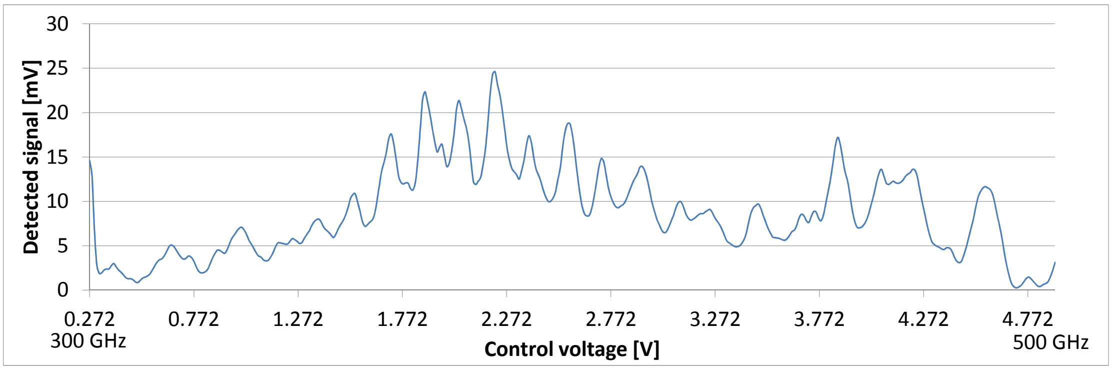

Figure 3.8: A nitrogen spectrum in terms of control voltage vs output voltage from the Golay cell. The voltage span corresponds to a full frequency sweep over 300-500 GHz. Note the very high sensitivity to small variations in the contol voltage. This sensitivity motivated the use of frequency modulation. [data/ctrl-to-signal]

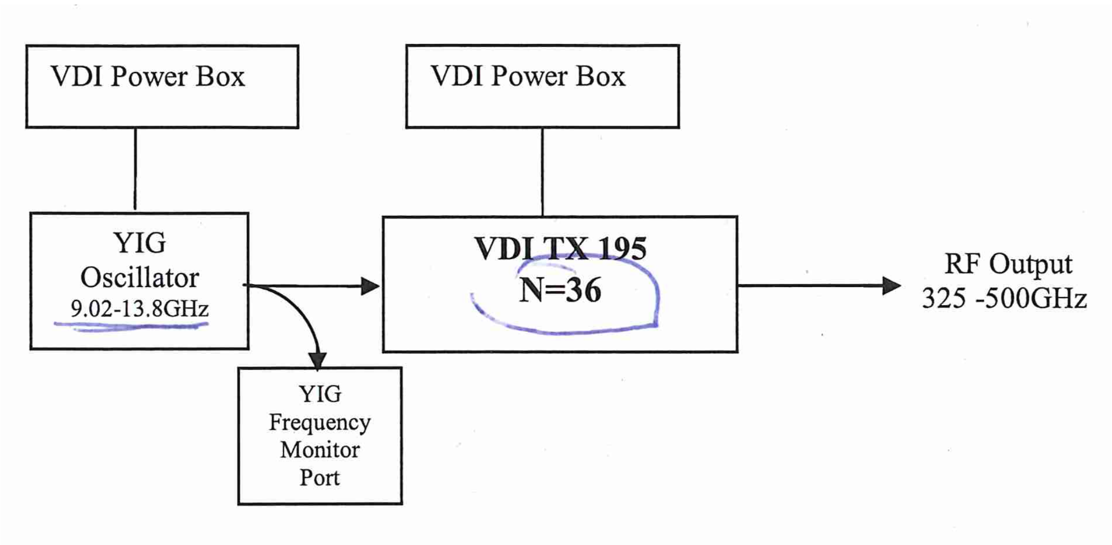

Figure 3.9: Sketch of the setup of the source, from VDI manual.

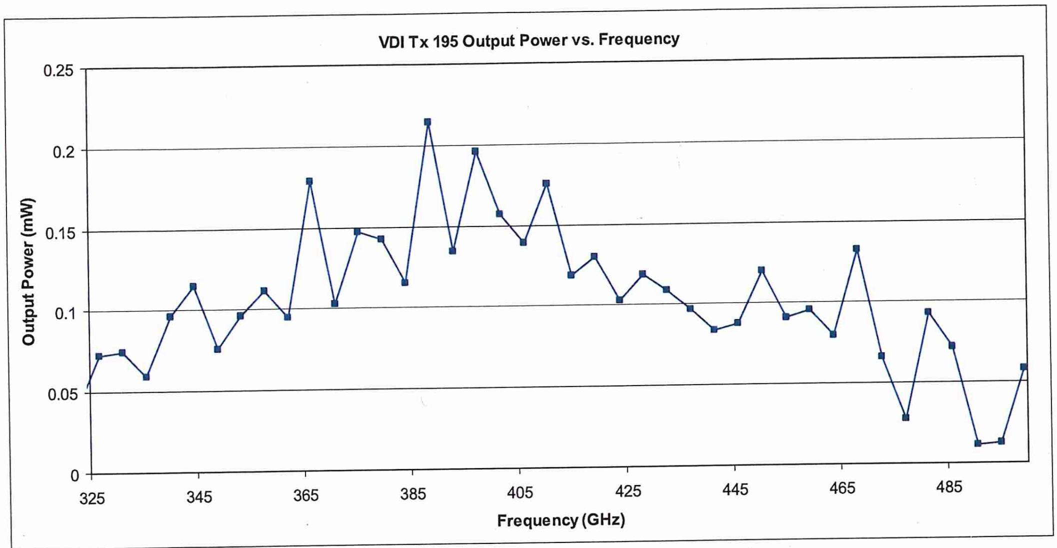

Figure 3: The product performance (output power vs. output frequency) is shown.

Figure 3.10: Source power output, from VDI manual.

3.2.2 Detector: Golay cell

The detectors were Golay cells with beam collimators, from Tydex. The Golay cell is a detector for IR, also usable in the THz range. Its principle of operation was first described by Golay [1947], hence its name. The device contains a material absorbing EM radiation within the relevant frequency range, producing heat. The absorber is placed in a sealed compartment of gas, sealed at one end by a transparent window and at the other by a flexible membrane. A mirror is attached to the outside of the membrane, and a photocell observes it. When the absorber heats up, heat is transferred to the gas, which expands. The flexible membrane moves in response to the pressure change, and the photocell detects this by measuning the change in reflected light from the membrane. The signal of the photocell is the output signal. Due to its thermal-mechanical nature the Golay cell is sensitive to mechanical vibrations as well as thermal noise and has a modest response time, on the order of tens of milliseconds (Rogalski [2010], pp 157-158) and a modulation frequency of about 20 Hz. It is however cheap and robust. A sketch is shown in figure 3.11.

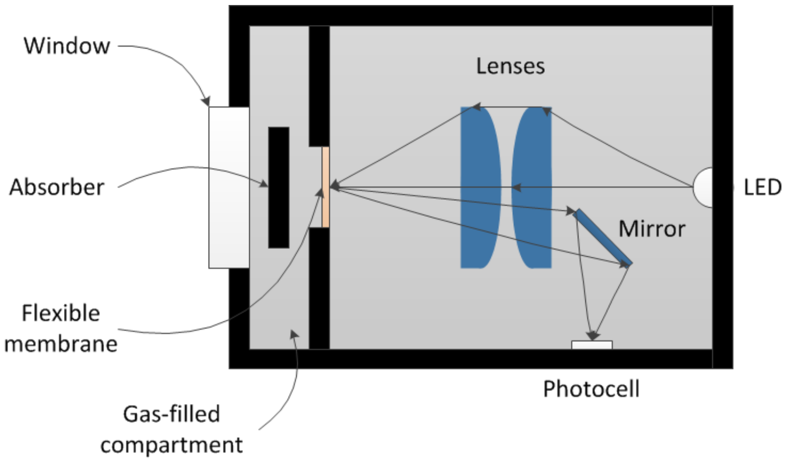

Figure 3.11: Sketch of the Golay cell

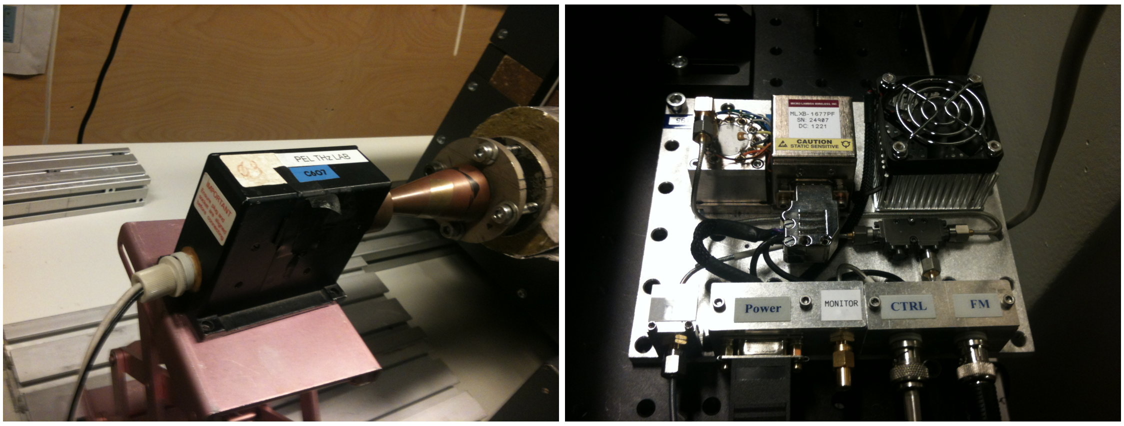

Figure 3.12: Left: Golay cell. Right: The microwave source

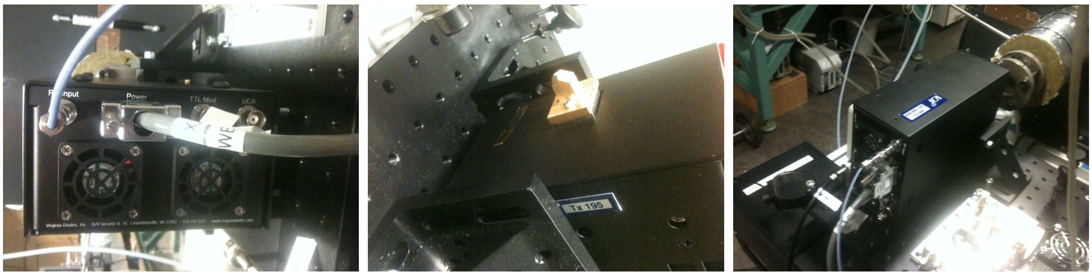

Figure 3.13: The Amplifier multiplier chain, concealed within a black box.

Table 3.2: Coefficients for the Antoine equation for H_2O, from DDBST [2013].

T range [C]	A	B	C
1-100	8.07131	1730.63	233.426
99-374	8.14019	1810.94	244.485

3.3 Humidity meter

To get a reference value for the humidity, a humidity meter was needed. The device chosen for this purpose was made in-house at the department of energy and the environment, and is described by Hermansson et al. [2011]. It could only be used in the lab environment where there was no tar in the gas, or for fluegas. The device monitors both temperature and relative humidity (RH), although the temperature readings are of little direct use in our case since the gas must be cooled before entering the device. They are however necessary to convert relative humidity to VMR (Volume mixing ratio, the ratio of the gas by volume). The RH measurement is done by use of chemically modified polymers that change capacitance depending on RH. The detector materials work at temperatures up to about 180^o C. To avoid condensation in the device it is kept at about 110^o C. Relative humidity is temperature dependent so VMR is extracted by multiplying the measured RH with the factor P_{sat}/P, where P is total pressure in the gas and P_{sat} saturation pressure. P is 750 mmHg and P_{sat} is given by the Antoine equation (Reid et al. [1987], chapter 7.3.1):

$$P_{\text{sat}}/P = 10^{(8.14019-(1810.94/(244.485+T)))}/750 \tag{3.4}$$

where pressure is in mmHg and temperature in Celsius. The Antoine equation is derived from the Clausius-Clapeyron equation and has two sets of coefficients, one below boiling point and one above so that RH can be defined at any temperature. The general form is:

$$\log_{10} P_{\text{sat}} = A - \frac{B}{C-T} \tag{3.5}$$

with coefficients for H_2O in the relevant units given in table 3.2.

3.4 Spectrum analysis

3.4.1 THz absorption by H_2O vapors

We have described the theory of spectral lines in section 2.3.2. We assumed a Lorentzian lineshape as a first guess, but at the high temperaure it might be necessary to use the Voigt function to get better results. Line parameters for the spectral range $0-40cm^{-1}$ were extracted from HITRAN and their contributions to the spectrum summed, since they might affect the transmission within in our spectral range. The thermodynamic partition function of water was obtained using piecewise polynomial interpolation of the values given by Vidler and Tennyson [2000]. MATLABs *nlinfit* was used to fit the parameters T and VMR in a least squares sense to the experimental data. The MATLAB function for the theoretical transmission is included as appendix A.

An alternative approach also pursued was to download a dataset from spectralcalc.com, which was also done. This data included the effects of line mixing and would be used to determine parameters via least-squares fitting.

According to HITRAN, water has 505 lines in the range 0-40 cm^{-1}. Most of these are very weak and can be disregarded. Values for the 48 strongest lines are provided in appendix B. We use only the two strongest lines at 383 and 448 GHz (12.68 and 14.44 cm^{-1}), but other lines contribute to the background so some of them must be considered. Figure 3.14 shows the H_2O lines in the intervals 10-16.7 cm^{-1} and 0-40 cm^{-1} with and without a cutoff intensity set at e^{-23}.

3.4.2 THz absorption by Carbon Monoxide

According to HITRAN, CO has 103 lines in 0-40 cm^{-1}. As for water, most are very weak and can be disregarded. Values for the 11 strongest lines are provided in appendix B. The line at 460 GHz is clearly visible and distinguishable from the nearby water lines and is the primary candidate for determining levels of CO. It is further commented in sections 4 and 5. Figure 3.15 shows the CO lines in the intervals 10-16.7 cm^{-1} and 0-40 cm^{-1} with and without a cutoff intensity set at e^{-23}.

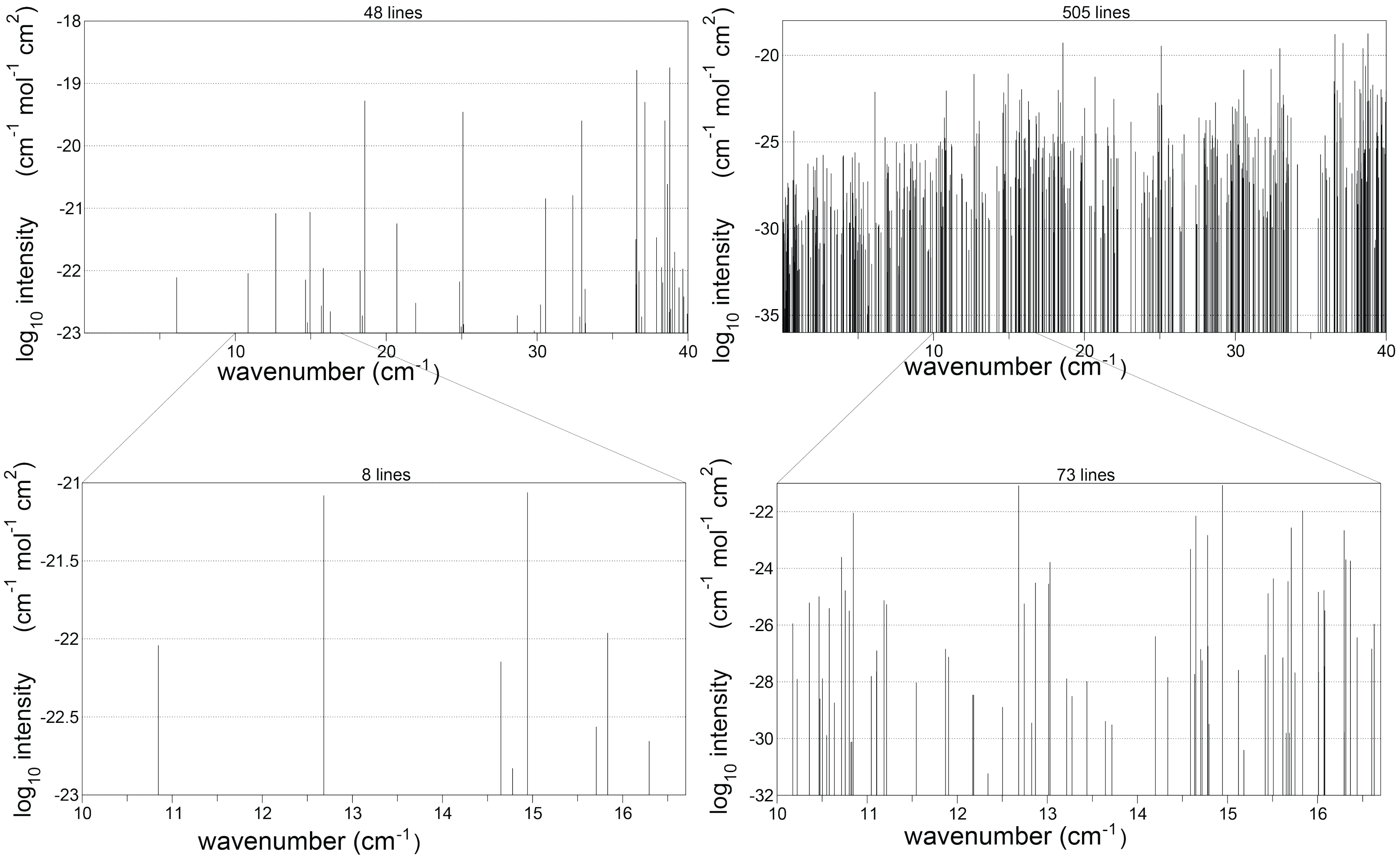

Figure 3.14: Line positions and intensities for H_2O. Upper left: 0-40 cm^{-1} with cutoff at intensity $< e^{-23}$. Upper right: 0-40 cm^{-1} with no cutoff. Lower left: 10-16.7 cm^{-1} with cutoff at intensity $< e^{-23}$ Lower right: 10-16.7 cm^{-1} with no cutoff. Compare figure 2.3.

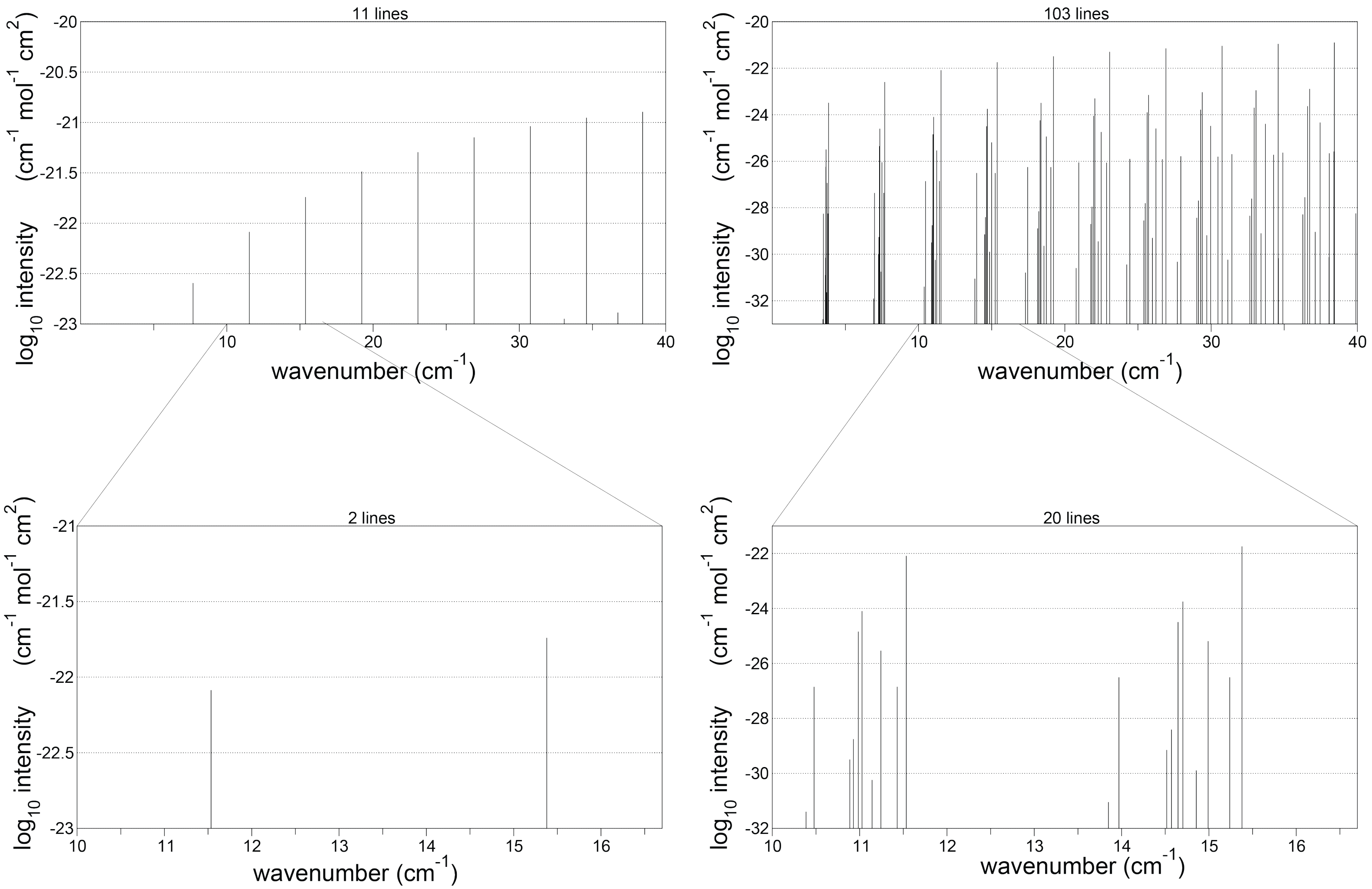

Figure 3.15: Line positions and intensities for CO. Upper left: 0-40 cm^{-1} with cutoff at intensity $< e^{-23}$. Upper right: 0-40 cm^{-1} with no cutoff. Lower left: 10-16.7 cm^{-1} with cutoff at intensity $< e^{-23}$ Lower right: 10-16.7 cm^{-1} with no cutoff. Compare figure 2.3.

4

Experimental methodology

4.1 Calibration

For obtaining a transmission spectrum, the backgrund transmission needs to be determined, then the transmission through the sample can be isolated from all other phenomena affecting absolute transmission. In figure 4.1 we show an example of how one calibration spectra and a raw measurement are used to produce the expected H_2O spectrum. In this case it is the spectrum of rawgas, where the H_2O-lines are the most prominent features.

Another type of measurement that was done is monitoring of specific frequencies over extended periods of time. In those cases, calibration was done by monitoring a pure N_2-spectrum for some time before the sample was let in, then dividing subsequent measurements with the average N_2 transmission at each frequency.

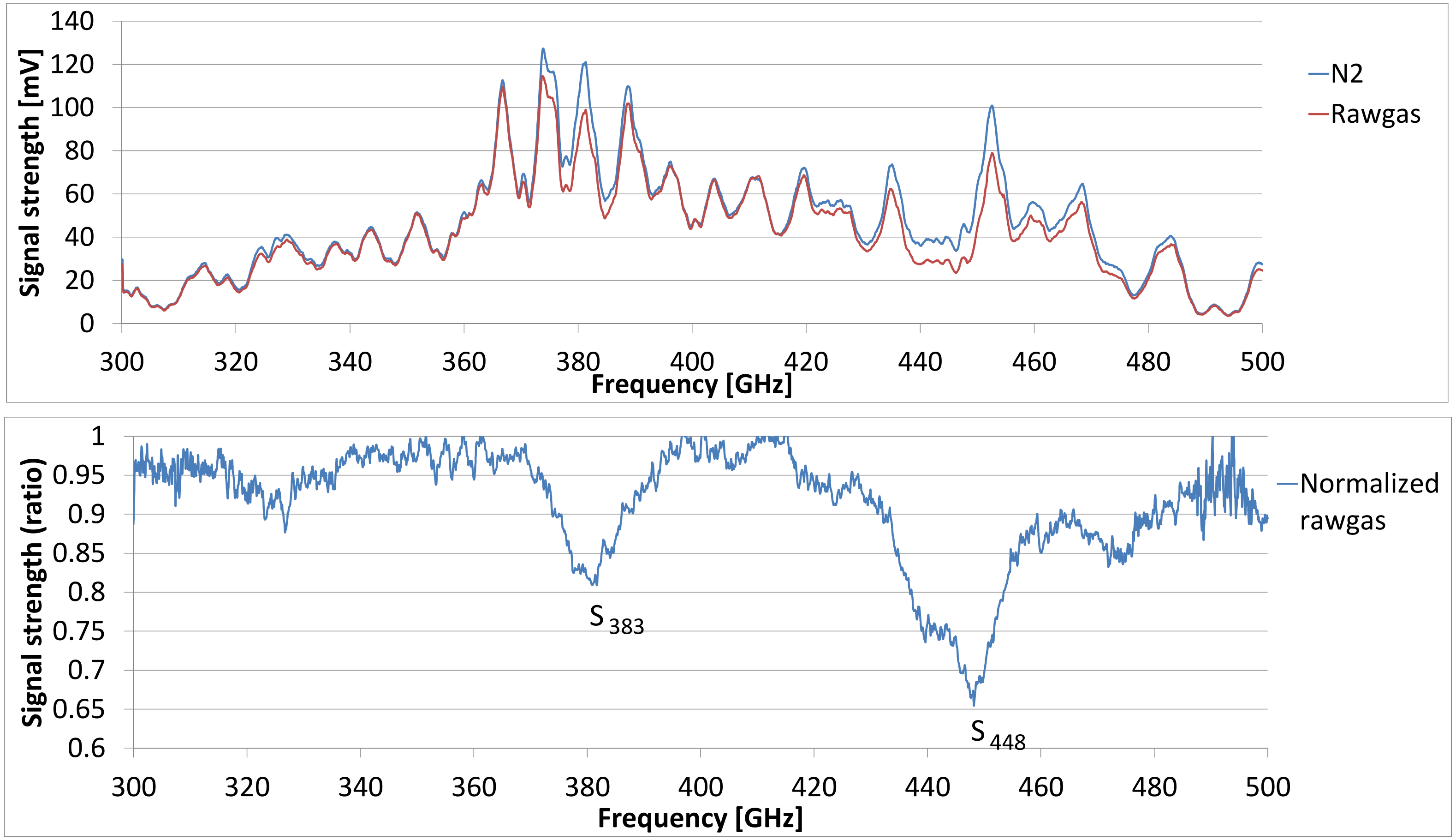

Figure 4.1: Top: Two raw measurements, one of N_2 which lacks spectral lines in this frequency range to be used for calibration, and one of gasifier rawgas. Bottom: The transmission spectrum formed by dividing the rawgasspectra by the calibration spectra. $VMR \approx 65\%$ and $T \approx 430^o$C. [data/rawspectra]

4.2 Laboratory H_2O measurements

Two ways of measuring H_2O were employed. A sweep of the entire spectrum, that can be used by fitting spectralcalc simulations to extract temperature and VMR. The other method was continous monitoring of a chosen set of frequencies at the line centers that should be enough to do the determination of VMR and T. These measurements where performed in parallell with humidity meter measurements using the device described in section 3.3. Measurements were made at 383 and 448 GHz, one at a time and also switching between the two lines for measuring them simultaneously. The transmissions and humidity measurements are summarized for several measurements of this type in table 4.1. One measurement of two lines simultaneously is shown in figure 4.2, this is the data called "1" in table 4.1. There was also a long timeseries taken where humidity was kept at a few closely spaced levels to determine if they could be differentiated from each other. The result is plotted in figure 4.3.

Table 4.1: Transmissions obtained at different humidity levels in two separate measurements of the type shown in figure 4.2. Errors are shown as one standard deviation. Measurement number indicates which of the two separate dataseries the entry comes from.

Measurement number	Transmission at 448 GHz	Transmission at 383 GHz	Humidity meter VMR [%]
1	0.684 ± 0.00870	0.784 ± 0.00428	95 ± 1.52
1	0.721 ± 0.00921	0.8 ± 0.00519	73 ± 0.99
1	0.751 ± 0.00836	0.813 ± 0.00502	57 ± 1.10
1	0.774 ± 0.00838	0.822 ± 0.00527	48 ± 1.10
1	0.781 ± 0.00830	0.825 ± 0.00509	41 ± 0.77
2	0.786 ± 0.00692	0.824 ± 0.00366	49 ± 1.19
2	0.76 ± 0.00979	0.819 ± 0.00259	57 ± 0.84
2	0.73 ± 0.00723	0.792 ± 0.00261	73 ± 0.90

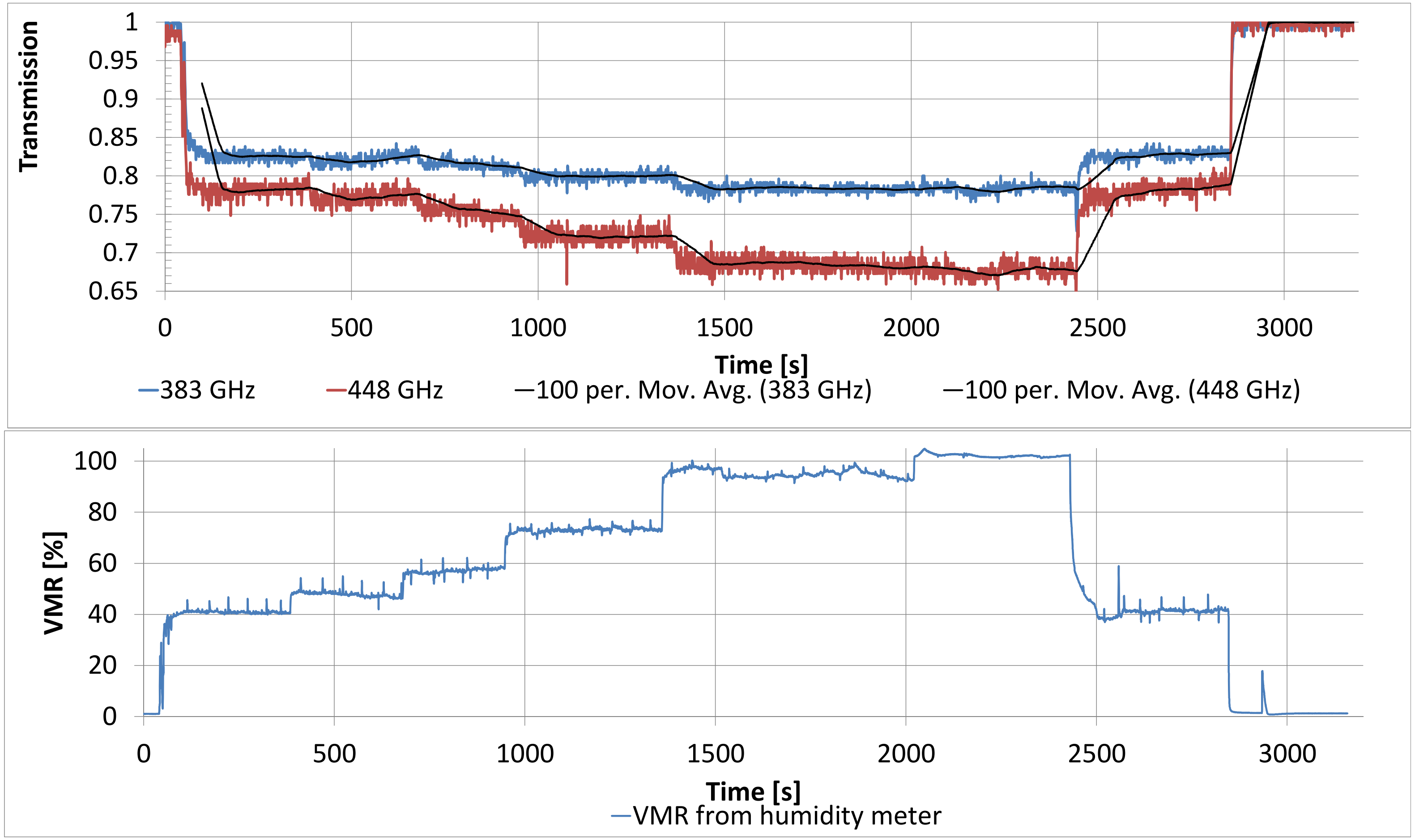

Figure 4.2: Top: the two water lines are plotted as functions of time, where the H_2O content is changed in steps. Bottom: the humidity meter gives the corresponding VMR. [data/twolines]

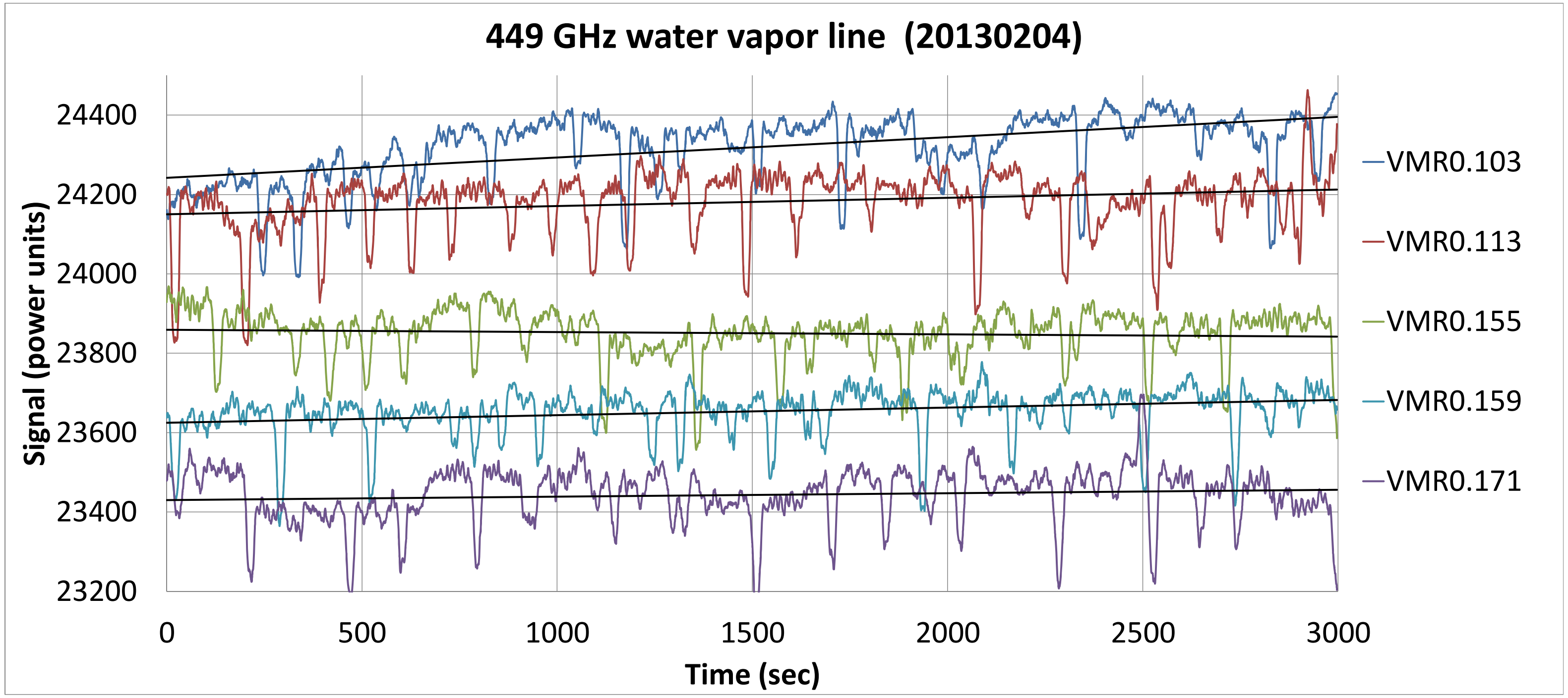

Figure 4.3: Laboratory measurement of transmission at 449 GHz over time for five humidity levels. The impulse-like objects are products of the humidifier, it seems to release steam in short pulses. Note that measurements with a difference in VMR as small as 0.4% can be clearly distinguished from each other. [/data/20130204]

4.3 Monitoring of H_2O and CO at the gasifier

Several spectra were taken where bottled CO and H_2O were introduced into the gas cell. H_2O and CO+H_2O is displayed in the figure 4.6. These give an indication of what one could expect to see in the rawgas, whose main features should be H_2O- and CO peaks.

A few spectra of the rawgas and fluegas were taken and are displayed in figures 4.4 and 4.5. The rawgas was kept at an underpressure of 0.8 atmospheres to prevent toxic leaks. This has some effect on the shape of lines, which must be accounted for when simulating the spectrum. The transmission at 448 GHz was monitored over time while changing the humidity just as in the laboratory case, the result is shown in figure 4.7. At the gasifier humidity is regulated by changing the input of steam to the process. Note the relatively fast oscillations in humidity level. This cannot be detected using the presently used, slower methods.

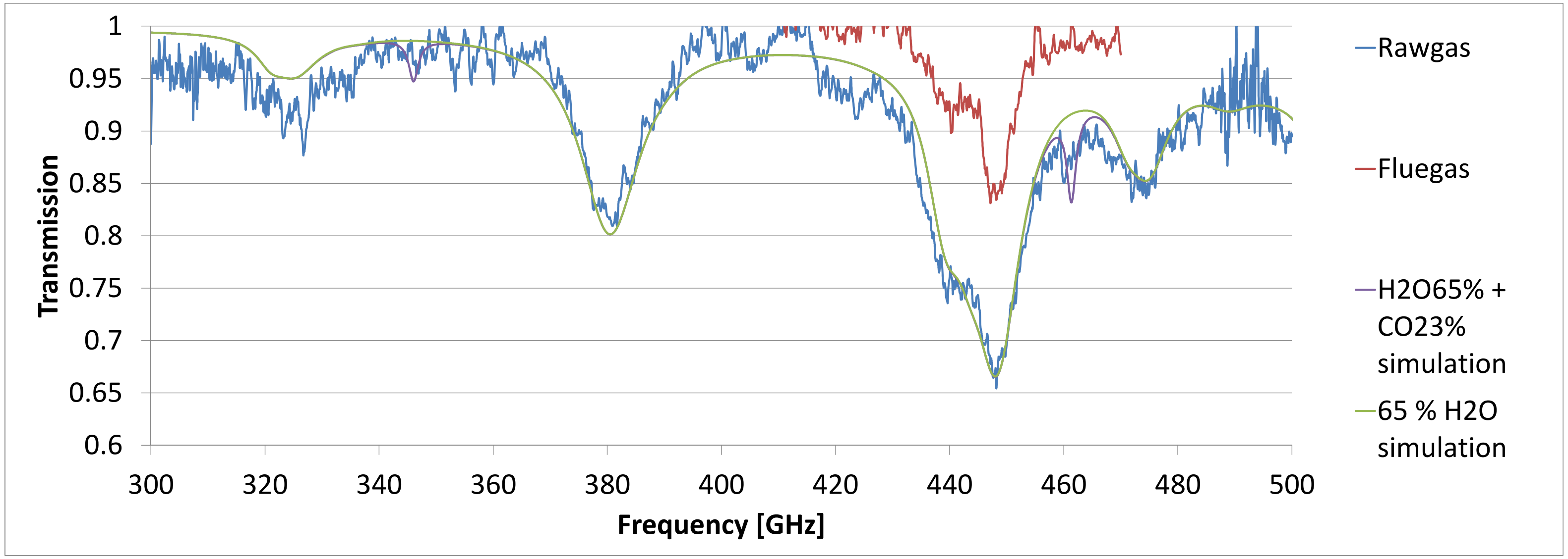

Figure 4.4: The spectrum of the rawgas, 300-500 GHz. Note the CO line at 460 GHz. Also included is a fluegas measurement at 410-470 GHz. Spectralcalc simulations for the rawgas are also included, compare table 2.1 of rawgas contents. [data/rawgasplot]

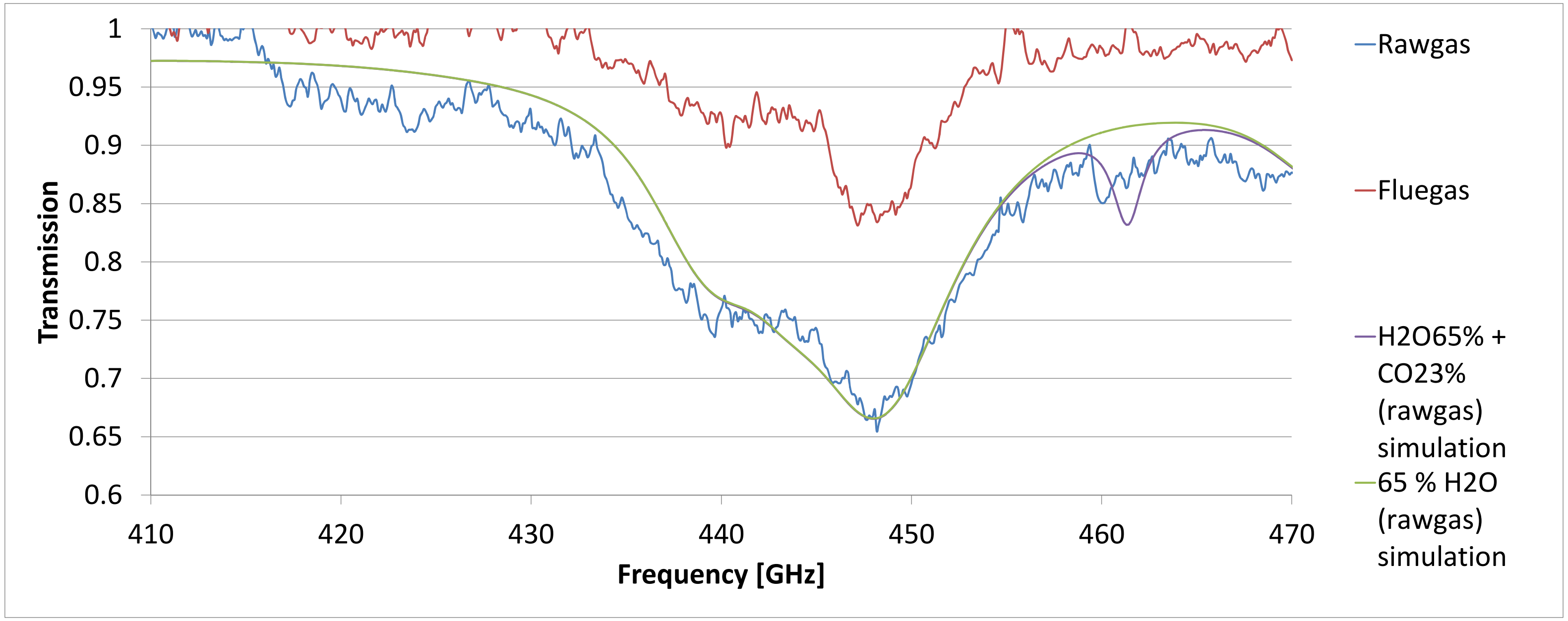

Figure 4.5: Raw and fluegas from the same measurement as above, zoomed in on the H_2O-line at 448 GHz.[data/rawgasplot]

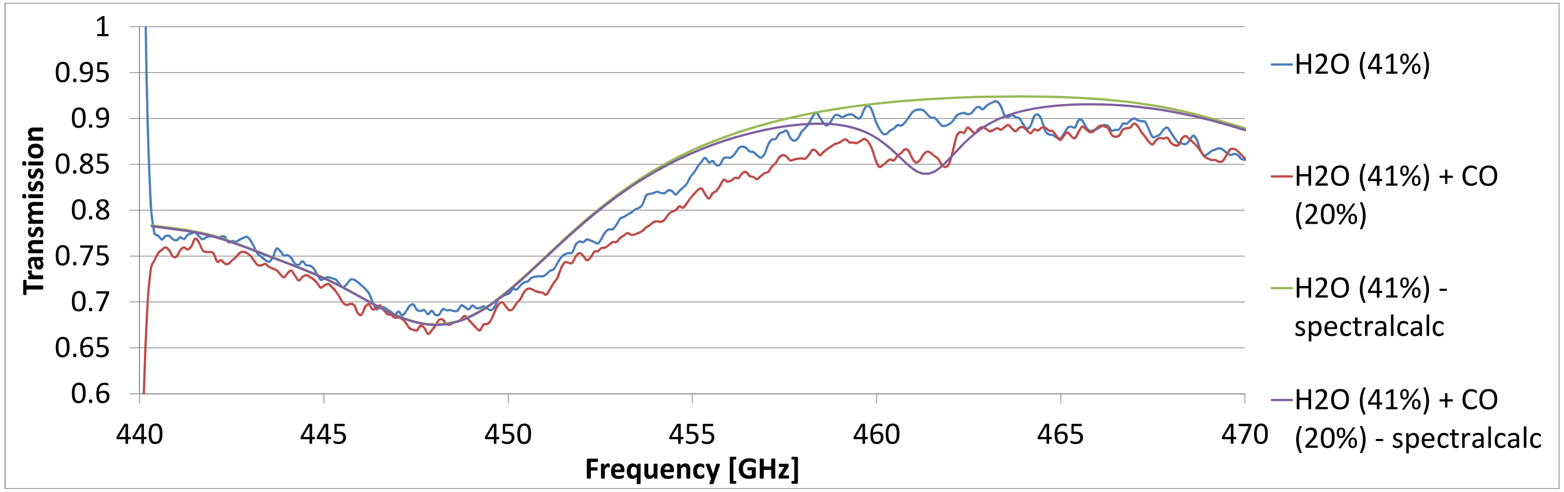

Figure 4.6: H_2O (41%) compared to H_2O (41%) and CO (20%). [/data/coandh2o]

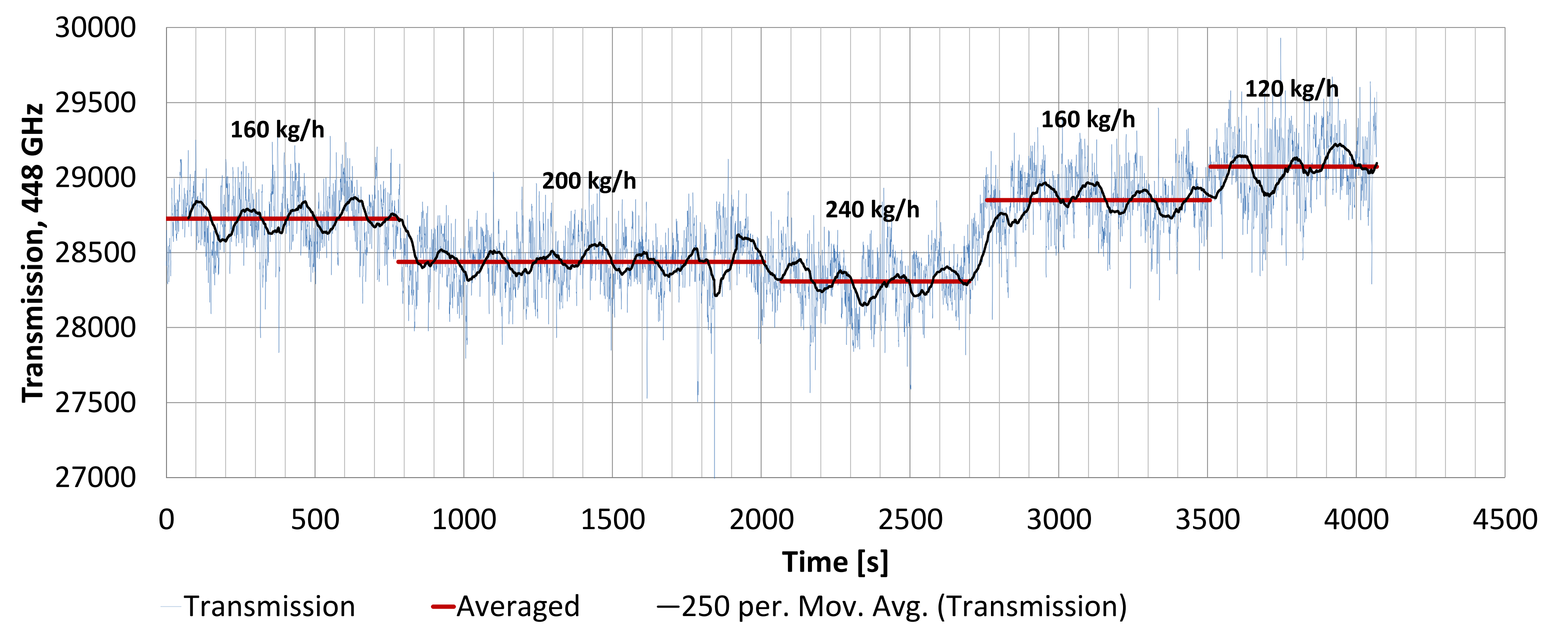

Figure 4.7: Measurement over time of the 448 GHz transmission at the gasifier. Varying the steam input of the process: 160, 200, 240, 160, 120 kg/h. [data/gasifier-humiditylevels]

4.4 Noise and drifts

The stability of the source over time was tested at room temperature, and at high temperature, to determine how heat leaking from the gas cell affects it. Significant drift, seemingly linear in time, was found at the higher temperature. More isolation was then achieved by moving the source further (10 cm) from the gas cell. The measurements were conducted by periodic sweeps of the entire frequency range, and without the reference detector. Figure 4.8,4.9 and 4.10 show the results. Noise in the lab environment was mostly below 2% and often below 1% of total signal strength at an integration time of 100 ms, and apparently consisted of white noise.

Figure 4.11 shows a representative plot of noise over the entire frequency range, in the lab. The noise level at the gasifier was about 2% of signal strength at integration time 100 ms, as shown in figure 4.12. At the ends of the operating range of the source, signal strength is close to zero and thus noise dominates. This can be clearly seen in the graphs. Numerous long duration scans at a single frequency were conducted for determining the precision and required integration time for the vapor measurement, both at gasifier and lab.

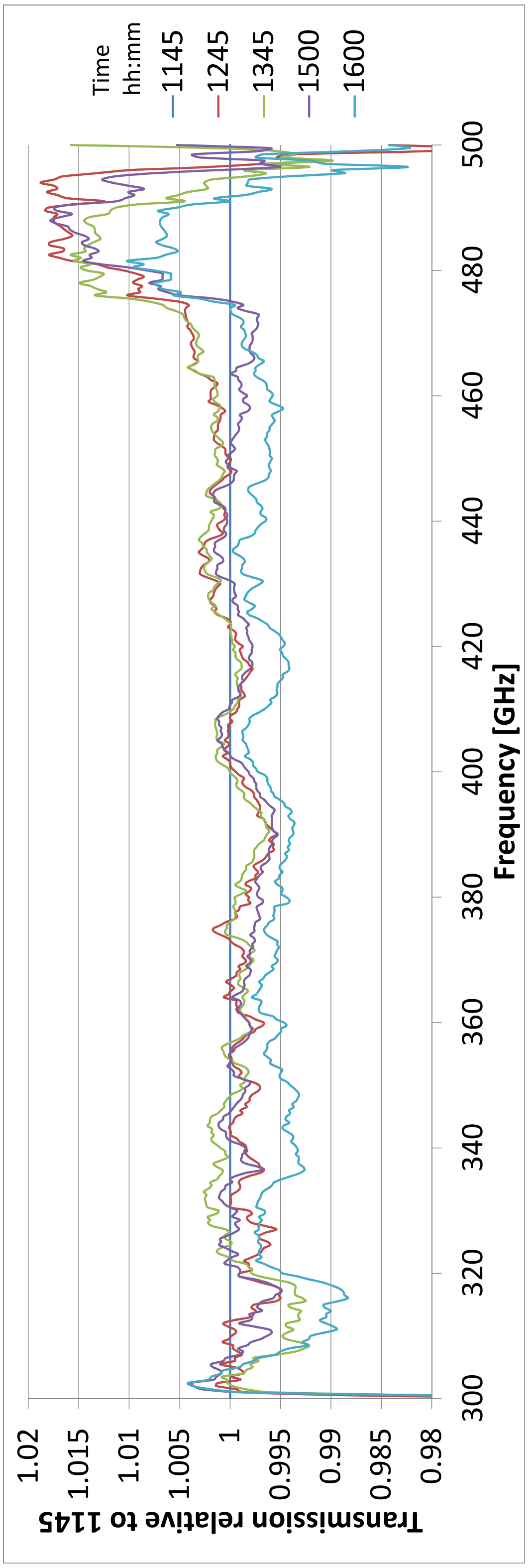

Figure 4.8: N_2 spectra taken over a period of four hours for the gas cell at room temperature and normalized to the first one of them. Moving average over 15 GHz.[data/drifts/book3-20130311]

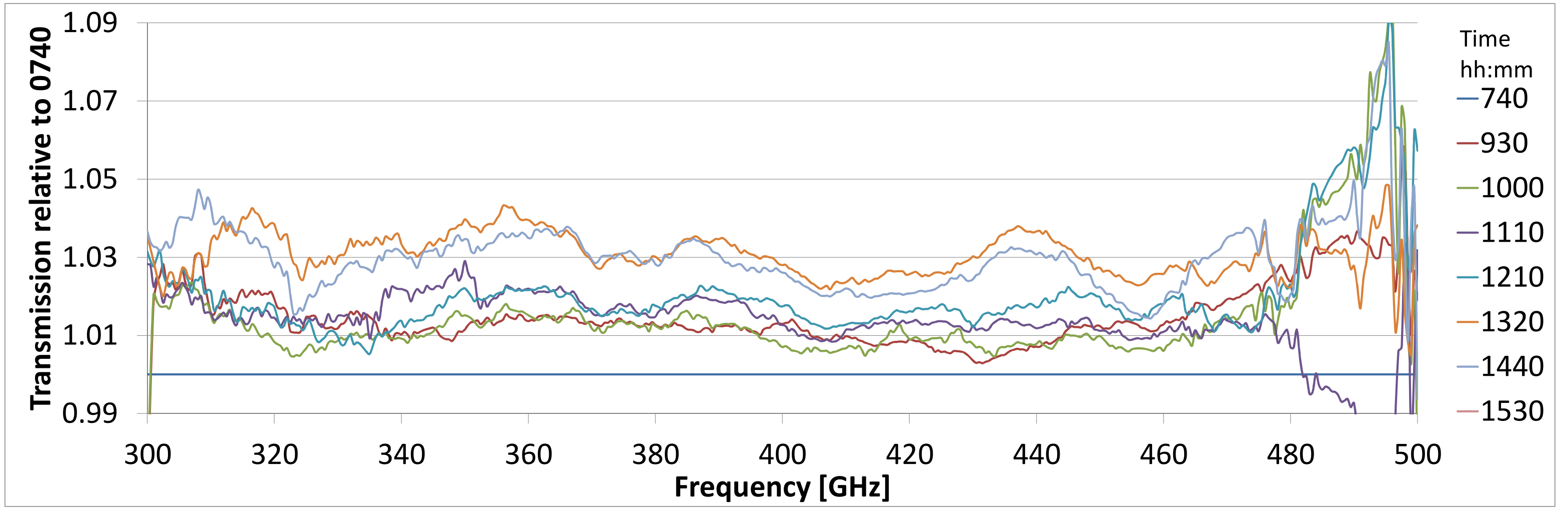

Figure 4.9: N_2 spectra taken over a period of eight hours at high temperature (oven at 600 C) and normalized to the first one of them. The legend shows the time that the corresponding measurement was taken. Moving average over 15 GHz.[data/drifts/book1-20130312]

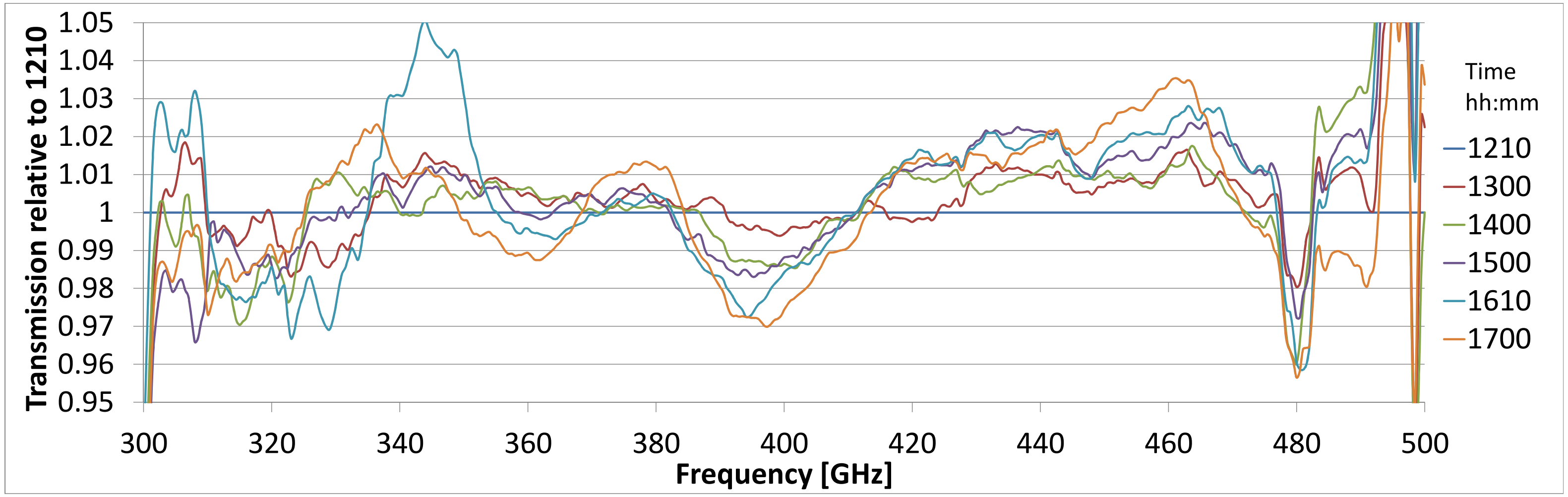

Figure 4.10: N_2 spectra taken over a period of five hours at high temperature (oven at 600 C) and normalized to the first one of them, with better thermal isolation (10 cm more air between source and gas cell) than in figure 4.9. Moving average over 15 GHz.[data/drifts/book2-20130327]

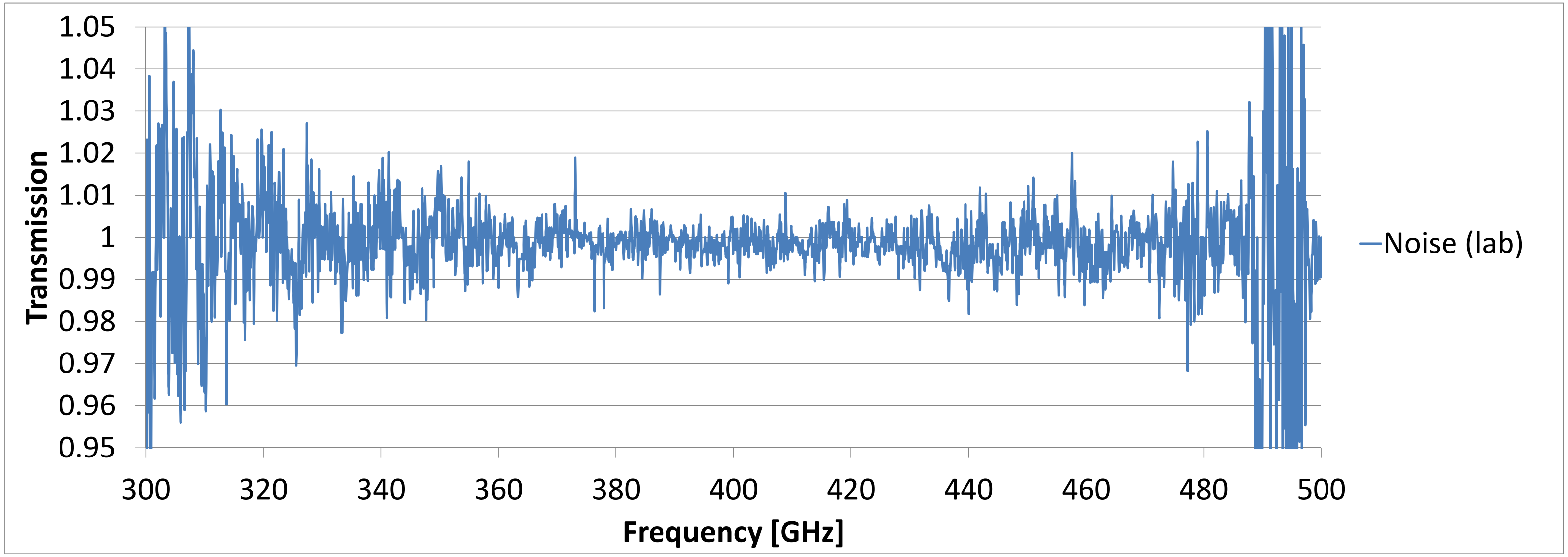

Figure 4.11: Noise plot in the lab obtained by division of two subsequent N_2-spectra. Integration time 100 ms. Note that signal strength approaches zero at the ends of the spectrum, causing signal-to-noise ratio to decrease. In this plot no smoothing has been used. [data/noise]

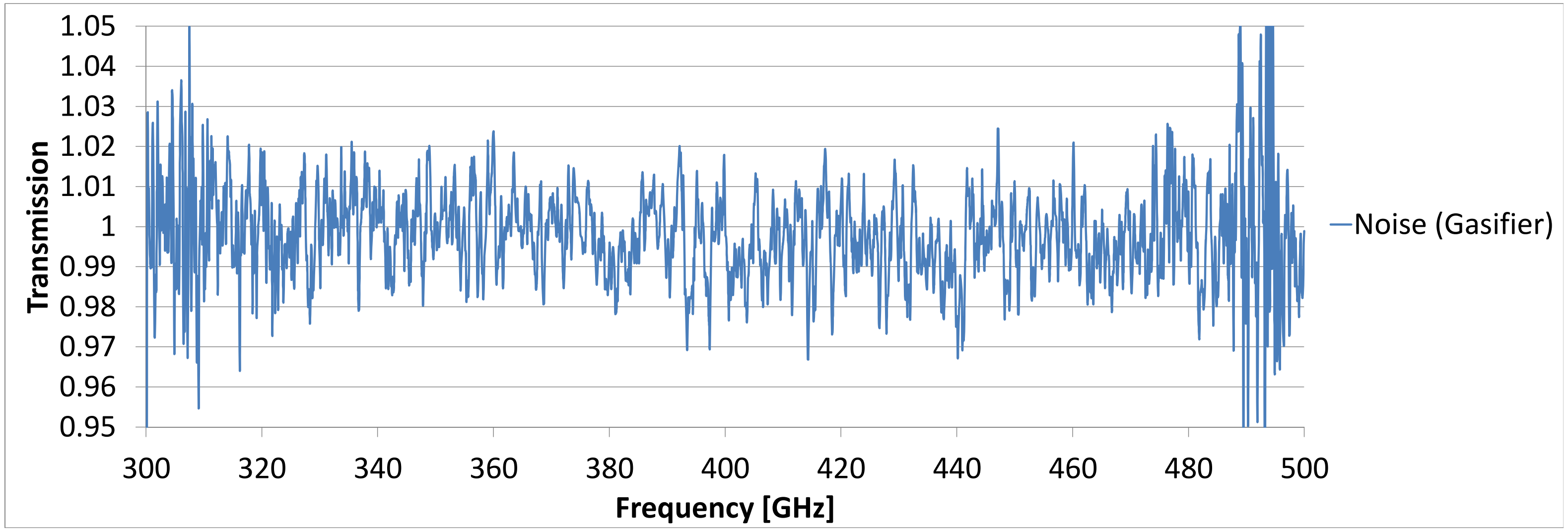

Figure 4.12: Noise plot at the gasifier obtained by division of two subsequent N_2-spectra. Integration time 100 ms. In this plot no smoothing has been used. [data/noise]

5

Discussion

5.1 Detection of H_2O

We have seen in figure 4.3 that the system can detect small differences in H_2O VMR in the lab, as small as 0.5% and probably smaller with sufficient time. Figure 4.7 indicates that the system detects changes in humidity at the gasifier as well. To determine the humidity level from the detected transmission, we need to simulate line strengths as described previously.

The effects of line mixing seem to be significant enough to make our line-by-line model ineffectice for full spectrum simulation. Instead, we downloaded simulated spectra from SpectralCalc.com to get an array of transmission values for temperatures in the range 373 K to 1073 K in steps of 20 K, VMRs in the range 0% to 100% in steps of 5% and wavelengths from 600 to 1000 μm in steps of 0.4 μm. MATLABs *interp3* interpolation function could then be used to extract values between these points.

Using the data shown in figure 4.2, the two known parameters of transmission and VMR can be used to extract the temperature by use of the plot in figure 5.1, which is line-by-line simulated transmission as function of temperature for the VMR given in the middle plot. One can pinpoint the correct ration between peak amplitudes between the two black lines inserted inte the plot. This is here shown for one of the humidity levels but is repeatable as made clerar in table 5.1. Very high humidity levels give condensation problems in the humidity meter but at intermediate levels the procedure seems to work quite well. In figure 5.2 the procedure for determining temperature is illustrated for the spectralcalc data, which gives a large inconsistency in temperature between the two different spectral lines. The error in the calculated temperature can be estimated as $\Delta T = \frac{dT}{dS}\Delta S$ where S is the transmission. These values are included in the table 5.1.

As shown in the figures 5.1 and 5.2 below, spectralcalc data gave inconsistent results when applied to the measured values of table 4.1. Line-by-line model gave less inconsistent results, but we show in figure 5.7 that it does not fit well with the spectra from frequency sweeps. Thus there might be an error in the measurement of the two line centers used here.

For the system to be operational however we need not only determine temperature for known transmission and humidity, we need to determine both temperature and humidity from only the transmission data. This was tried by extending the fitting procedure to the VMR-axis as well. This gave results that deviated a lot from expected values, probably because of the low resolution used in the fitting due to longer computation time compared to the fitting of one variable at a time. The MATLAB program is shown in appendix D.3. Using it to extract T and VMR from the measurements in table 5.1 gives the output shown in table 5.2.

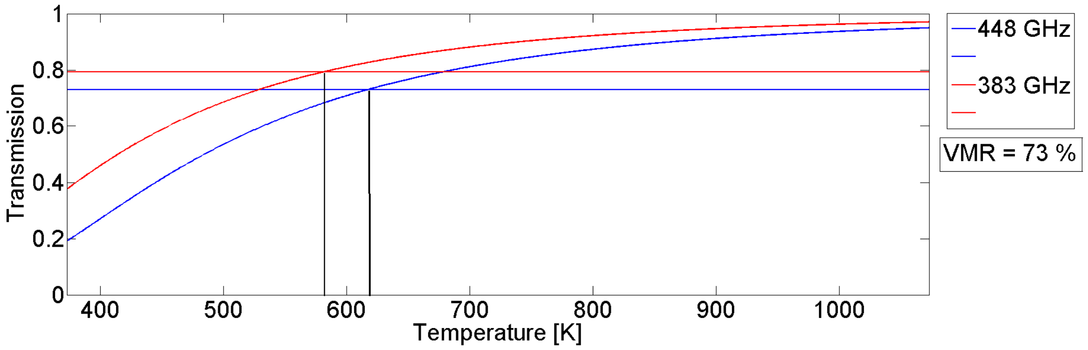

Figure 5.1: Transmission as function of temperature calculated by the line-by-line-model for the VMR of 73% detected in the measurements of figure . The black lines show where the measured transmissions intersect the simulation, giving the temperature. The values of T should coincide, but do not. Precise estimates from a least-squares fit for several measurements of this type are shown in table 5.1. [data/temp_humidity]

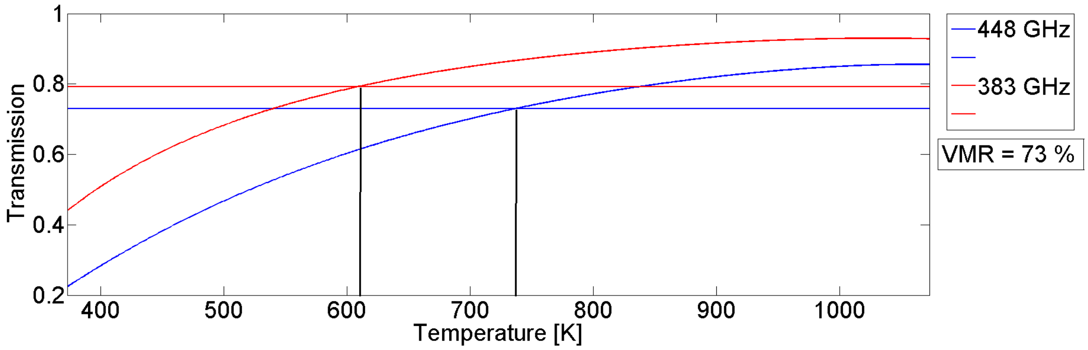

Figure 5.2: Transmission as function of temperature calculated by Spectralcalc for the VMR of 73% detected in the measurements of figure . The black lines show where the measured transmissions intersect the simulation, giving the temperature. The values of T should coincide, but do not. The temperatures differ much more than above. [data/temp_humidity]

Table 5.1: Temperature estimations using least-squares from the data in table 4.1. The calculation is shown in appendix D. Errors are given as one standard deviation. The last column shows how VMR is calculated assuming the calculated temperature and measured transmissions.

series #	Transmission at 448 GHz	Transmission at 383 GHz	Measured VMR [%]	Calculated T [K] at 383 GHz	Calculated T [K] at 448 GHz	Calculated T [K]	Calculated VMR [%]
1	0.684 ± 0.00870	0.784 ± 0.00428	95 ± 1.52	564 ± 4.0553	569 ± 5.6295	567 ± 4.842	92 ± 8.1
1	0.721 ± 0.00921	0.8 ± 0.00519	73 ± 0.99	604 ± 5.8648	611 ± 7.2912	608 ± 6.578	71 ± 5.4
1	0.751 ± 0.00836	0.813 ± 0.00502	57 ± 1.10	648 ± 6.6442	659 ± 7.9778	654 ± 7.311	56 ± 3.7
1	0.774 ± 0.00838	0.822 ± 0.00527	48 ± 1.10	683 ± 7.8814	701 ± 9.2126	692 ± 8.547	47 ± 3.2
1	0.781 ± 0.00830	0.825 ± 0.00509	41 ± 0.77	710 ± 8.0590	727 ± 9.8414	719 ± 8.950	40 ± 2.8
2	0.786 ± 0.00692	0.824 ± 0.00366	49 ± 1.19	683 ± 5.7437	712 ± 7.9477	698 ± 6.850	48 ± 2.6
2	0.76 ± 0.00979	0.819 ± 0.00259	57 ± 0.84	656 ± 3.5908	668 ± 9.7661	662 ± 6.679	56 ± 3.5
2	0.73 ± 0.00723	0.792 ± 0.00261	73 ± 0.90	595 ± 2.9828	619 ± 6.3363	607 ± 4.660	70 ± 3.8

Table 5.2: The result when fitting both T and VMR using the program in appendix D.3, and the same data as in the table above.

Series #	1	1	1	1	1	2	2	2
Measured VMR [%]	95	73	57	48	41	49	57	73
Calculated VMR [%]	85	55	35	20	20	10	40	30
Calculated T [K]	573	633	713	803	813	893	703	703

5.2 Detection of CO

While CO is clearly visible in the rawgasspectra of figure 4.4 and 4.5 the precision with which it can be detected has not been determined.

5.3 Noise and drifts

The measurements in figure 4.8,4.9 and 4.10 indicate that the room temperature drift is less than 0.25% per hour, small compared to the noise. At higher temperature, the signal drifts at a rate of up to 0.6% per hour. When the heat was reduced by moving the source further from the gas cell, the magnitude of drifts has reduced to about 0.4% per hour, indicating that thermal isolation is appropriate to achieve good stability.

The relation of noise to integration time was tested in the lab with pure nitrogen at a temperature of $308/325^{o}C$ as shown by the thermocouples at inlet/outlet and at a frequency 383 GHz. Measurements were taken with a time constant of 300 ms once per second for an hour. Figure 5.4 shows the Allan variance of the measurement. The Allan variance of the 449 GHz line taken at the gasifier, for rawgas, is shown in figure 5.6 and the raw signal in figure 5.5. That measurment was taken with 100 ms integration time and one point per 300 ms.

Allan variance is a measure of how RMSD[1] relates to integration time. The Allan M-sample variance is defined as:

$$\sigma_y^2(M,T,\tau) = \frac{1}{M-1}\Big(\sum_{i=0}^{M-1}\Big[\frac{x(iT+\tau)-x(iT)}{\tau}\Big]^2 - \frac{1}{M}\Big[\sum_{i=0}^{M-1}\Big[\frac{x(iT+\tau)-x(iT)}{\tau}\Big]\Big)\tag{5.2}$$

Where M is number of samples, x is the data and T is the time. Integration time is then $M\tau$. We can see in the figure that the optimal integration time is reached after only 20-30 seconds. If there were no drifts, there would be no optimum but an exponentially decreasing payoff for increasing integration time.

---

[1]

$$\text{RMSD} = \sqrt{\frac{1}{n}\sum_i[(x_i-\bar{x})^2]}\tag{5.1}$$

where $\bar{x}$ is the signal mean, used as the ”true” signal.

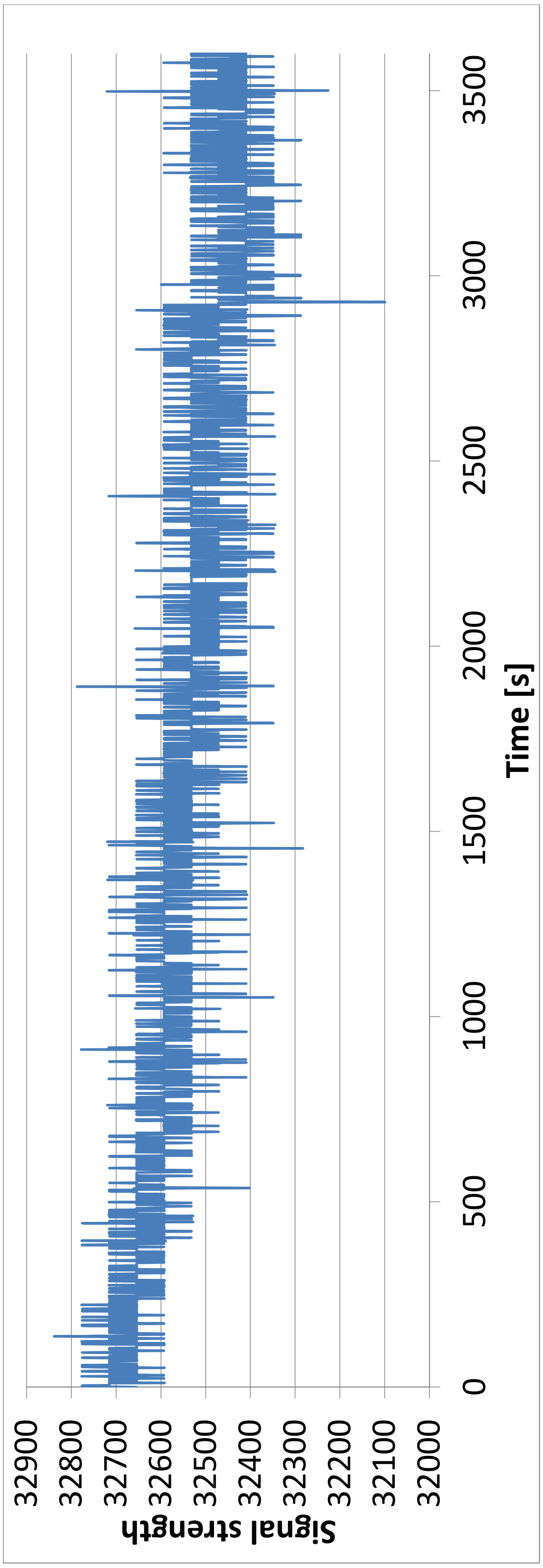

Figure 5.3: An N_2 measurement at 383 GHz with 300 millisecond integration time and one data point taken per second, in the lab.[data/rmsd]

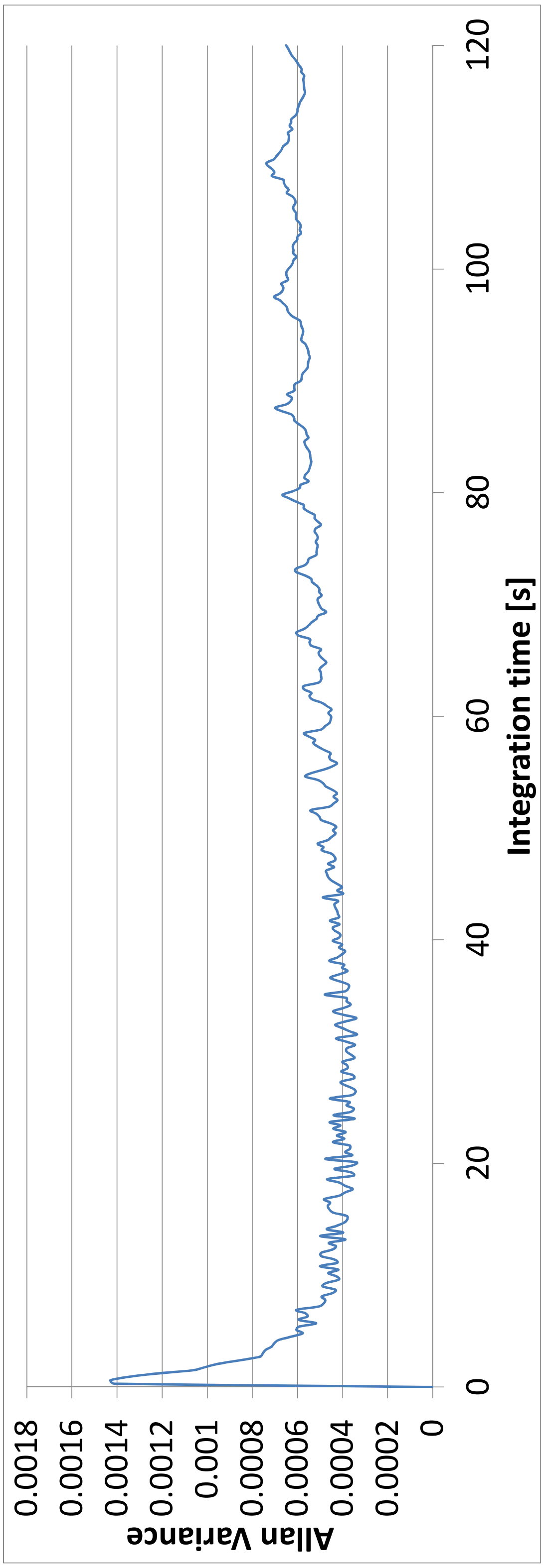

Figure 5.4: Allan variance of the above signal.[data/rmsd]

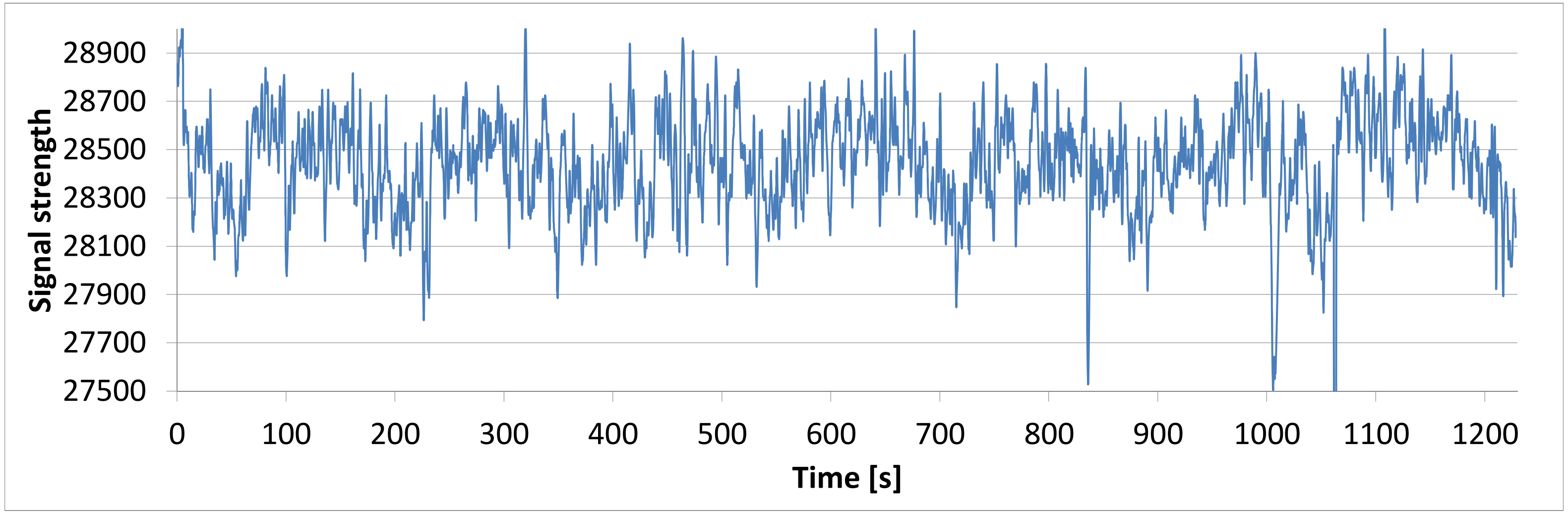

Figure 5.5: The 449 GHz line from rawgas at the gasifier (200 kg/h of H_2O), monitored for 1200 seconds. 100 millisecond integration time and one data point taken per 300 milliseconds.[data/rmsd]

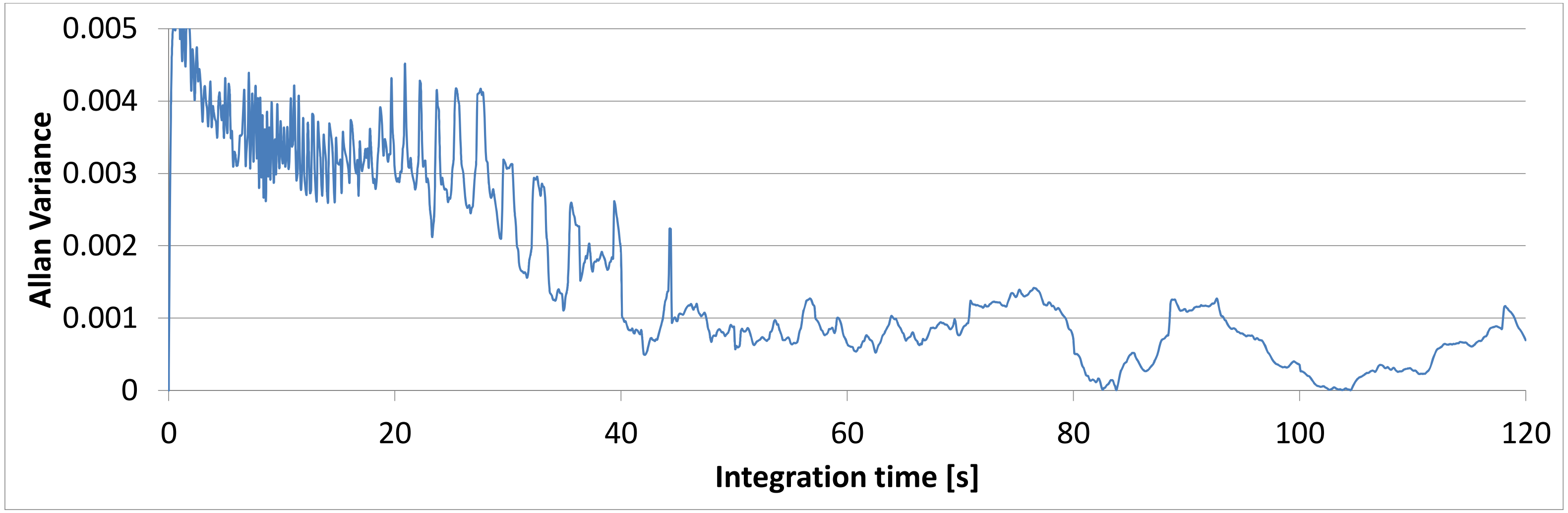

Figure 5.6: Allan variance of the above signal. [data/rmsd]

5.4 Other issues

5.4.1 Temperature gradient and thermocouples

The thermocouples used to determine gas temperature at the inlet and outlet of the cell proved to be quite unpredictable. This is so for several reasons. First, they couple radiatively to the hot steel of the waveguide, leading to exaggarated temperatures. On the other hand, they are not very exactly aligned to measure the temperature at representative points, such as the exact center of the gas flow. Patterns of turbulence inside the cell may have an unknown impact. It is thus not surprising that the thermocouple readings were only very roughly related to temperatures estimated from the spectra.

One effect seen in the thermocouple measurements is worthy of consideration however. Gas enters the cell from 200^oC heated tubes, coming into contact with a hotter environment. It starts heating in the pre-heating tube spiralling along the gas cell. Then it exits, possibly not yet in thermal equilibrium, into the gas cell. Thus a temperature gradient of significant magnitude can be expected to exist in the cell. Its magnitude is not in any simple way related to the various parameters of the gas. One could have expected that higher vapor contents would lower the magnitude of the gradient due to higher heat capacity, but on the other hand vapor content was regulated by decreasing N_2 flow, meaning that the gas had longer time to gain heat from the walls of the waveguide. Higher mass flow would introduce turbulence at lower humidity levels, which would promote heat transfer from wall to gas.

A third insertion point for a thermocouple straight into the middle of the gas cell was tested and gave a temperature varying around 600^o C, the temperature of the oven. This is probably a good reason to believe the measurements at the other two insertion points were of little relevance. Spectroscopy cannot determine the temperature gradient but only the average temperature.

5.4.2 Line-by-line model vs LINEPAK

The line-by-line simulation did not perform as good as the Spectralcalc simulations to reproduce measured spectra. When trying to extract parameters, spectralcalc data gave inconsistent results while the line-by-line algorithm produced more consistent results. A comparison of the two methods is shown in 5.7. Since the Spectralcalc data worked well for fitting to the full spectra, we would expect it to produce consistent results. There might have been a systematic error in the measurement of two lines simultaneously that can explain this problem.

5.5 Usability of the system

The system can detect water in a matter of seconds in the environment of the lab. We have also shown that waterlines in the rawgas can be detected, and the required integration time is on the order of 2 minutes. The presence of CO can be simultaneously detected with an as yet unclear accuracy. For these experiments an expensive THz source

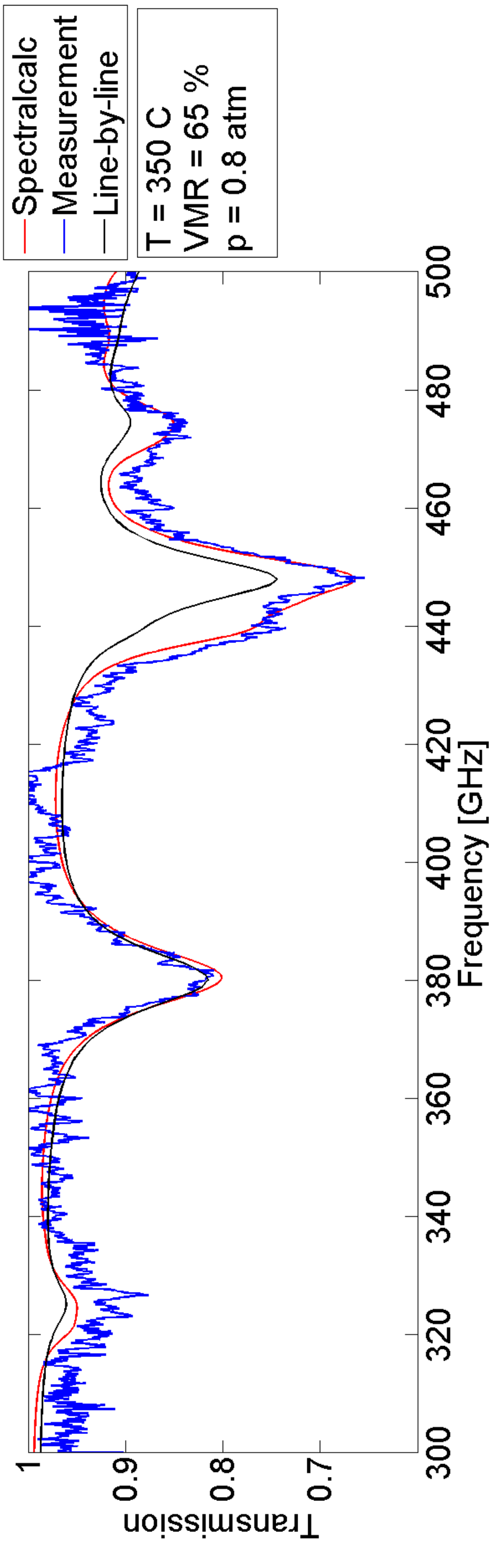

Figure 5.7: A comparison of rawgas measurment, spectralcalc and line-by-line simulation. [data/comparison]

has been used, but in an applied system a cheaper set of a few fixed-frequency sources could be used. This would reduce the cost drastically. It still remains to be determined how many frequencies need to be monitored, but at least three separate ones for water. Since temperature will be determined by the water measurement, one peak from each additional substance would suffice.

Bibliography

Craig F. Bohren and Donald R. Huffman. *Appendixes: Computer Programs*, pages 475–476. Wiley-VCH Verlag GmbH, 2007. ISBN 9783527618156. doi: 10.1002/9783527618156.app1. URL `http://dx.doi.org/10.1002/9783527618156.app1`.

S. Cherednichenko, A. Hammar, S. Bevilacqua, V. Drakinskiy, J. Stake, and Alexey Kalabukhov. A room temperature bolometer for terahertz coherent and incoherent detection. *Terahertz Science and Technology, IEEE Transactions on*, 1(2):395–402, 2011. ISSN 2156-342X. doi: 10.1109/TTHZ.2011.2164654.

Stefan Dahlgren, Anna Liljeblad, Jenny Cerruto, Nohlgren Ingrid, and Starberg Katarina. *Realiserbar biogaspotential i Sverige år 2030 genom rötning och förgasning.* WSP, Stockholm, 2013.

DDBST. Dortmund data bank saturated vapor pressure online calculator, 2013. URL `http://ddbonline.ddbst.de/AntoineCalculation/AntoineCalculationCGI.exe?component=Water`.

Marcel J. E. Golay. Theoretical consideration in heat and infra-red detection, with particular reference to the pneumatic detector. *Review of Scientific Instruments*, 18 (5):347–356, 1947. doi: 10.1063/1.1740948. URL `http://link.aip.org/link/?RSI/18/347/1`.

A. Gomez-Barea and B. Leckner. Modeling of biomass gasification in fluidized bed. *Progress in Energy and Combustion Science*, 36:444–509, 2010. ISSN 0360-1285. doi: 10.1016/j.pecs.2009.12.002.

Nachappa Gopalsami, Sasan Bakhtiari, Thomas W. Elmer II, and Apostolos C. Raptis. Application of millimeter-wave radiometry for remote chemical detection. *IEEE transactions on microwave theory and techniques*, 56(3):700–709, 2008.

Nachappa Gopalsami, Apostolos C. Raptis, H. T. Chien, A. Heifetz, and E. R. Koehl. Millimeter wave detection of nuclear radiation: An alternative detection mechanism. *Review of scientific instruments*, 80, 2009. ISSN 0034-6748.

Larry L. Gordley, Benjamin T. Marshall, and D. Allen Chu. Linepak: Algorithms for modeling spectral transmittance and radiance. *Journal of Quantitative Spectroscopy and Radiative Transfer*, 52(5):563 – 580, 1994. ISSN 0022-4073. doi: 10.1016/0022-4073(94)90025-6. URL `http://www.sciencedirect.com/science/article/pii/0022407394900256`.

Jean-Michel Hartmann, Christian Boulet, and Daniel Robert. *Collisional effects on molecular spectra: laboratory experiments and models, consequences for applications.* Elsevier Science, 2008.

Eugene Hecht. *Optics (4th Edition).* Addison Wesley, 4 edition, August 2001. ISBN 0805385665. URL `http://www.amazon.com/exec/obidos/redirect?tag=citeulike07-20&path=ASIN/0805385665`.

Sven Hermansson, Fredrik Lind, and Henrik Thunman. On-line monitoring of fuel moisture-content in biomass-fired furnaces by measuring relative humidity of the flue gases. *Chemical Engineering Research and Design*, 89(11):2470 – 2476, 2011. ISSN 0263-8762. doi: 10.1016/j.cherd.2011.03.018. URL `http://www.sciencedirect.com/science/article/pii/S0263876211001419`.

N.S. Hush and M.L. Williams. Carbon monoxide bond length, force constant and infrared intensity variations in strong electric fields: Valence-shell calculations, with applications to properties of adsorbed and complexed co. *Journal of Molecular Spectroscopy*, 50(1–3):349 – 368, 1974. ISSN 0022-2852. doi: 10.1016/0022-2852(74)90241-0. URL `http://www.sciencedirect.com/science/article/pii/0022285274902410`.

Philip Laven. Mieplot - a computer program for scattering of light from a sphere using mie theory & the debye series, May 2013. URL `http://www.philiplaven.com/mieplot.htm`.

K.N. Liou. *An Introduction to Atmospheric Radiation*, volume 84 of *International Geophysics*. Academic Press, 2002. doi: 10.1016/S0074-6142(02)80015-8. URL `http://www.sciencedirect.com/science/article/pii/S0074614202800158`.

Lorenzo Lori. *Theoretical Rotational-Vibrational Spectroscopy of Water.* PhD thesis, University of London, 2008.

Donald A. McQuarrie. *Quantum Chemistry.* University Science Books, Saulito, California, second edition, 2008.

Robert C Reid, John M Prausnitz, and Bruce E Poling. The properties of gases and liquids. 1987.

A. Rogalski and F. Sizov. Terahertz detectors and focal plane arrays. *Opto-Electronics Review*, 19(3):346–404, 2011. ISSN 1230-3402. doi: 10.2478/s11772-011-0033-3. URL `http://dx.doi.org/10.2478/s11772-011-0033-3`.

Antonio Rogalski. *Infrared Detectors, Second Edition.* CRC Press, 2010.

L.S. Rothman, I.E. Gordon, A. Barbe, D.Chris Benner, P.F. Bernath, M. Birk, V. Boudon, L.R. Brown, A. Campargue, J.-P. Champion, K. Chance, L.H. Coudert, V. Dana, V.M. Devi, S. Fally, J.-M. Flaud, R.R. Gamache, A. Goldman, D. Jacquemart, I. Kleiner, N. Lacome, W.J. Lafferty, J.-Y. Mandin, S.T. Massie, S.N. Mikhailenko, C.E. Miller, N. Moazzen-Ahmadi, O.V. Naumenko, A.V. Nikitin, J. Orphal, V.I. Perevalov, A. Perrin, A. Predoi-Cross, C.P. Rinsland, M. Rotger, M. Šimečková, M.A.H. Smith, K. Sung, S.A. Tashkun, J. Tennyson, R.A. Toth, A.C. Vandaele, and J. Vander Auwera. The {HITRAN} 2008 molecular spectroscopic database. *Journal of Quantitative Spectroscopy and Radiative Transfer*, 110(9–10):533 – 572, 2009. ISSN 0022-4073. doi: 10.1016/j.jqsrt.2009.02.013. URL `http://www.sciencedirect.com/science/article/pii/S0022407309000727`. <ce:title>HITRAN</ce:title>.

M Vidler and J Tennyson. Accurate partition function and thermodynamic data for water. *J. Chem. Phys.*, (113):9766–9771, 2000.

A

Line-by-line algortihm

This is the line-by-line algorithm referred to in the text. Function for extracting spectralcalc data provided at the end of the appendix for comparison.

```
function f = trans(p,vin)
T=p(1);
VMR=p(2);
v = vin*(1/29.9792); % Convert GHz to reciprocal cm
global offset params; % params is a set of HITRAN data
h = 6.63E-34; % Planck constant
c = 3E8; % speed of light
kb = 1.38E-23; % Boltzmann constant
NA=6.022E23; % Avogadro constant
R=8.2e-1; % Molar gas constant
l=1.0; % Length of gas cell
p0=1; % Reference pressure
p=1; % Pressure, atm
T0=296; % Reference temperature

% Loading the HITRAN data
n = params.n;
a0 = params.a0;
v0 = params.v0;
v02 = v0;
s = params.s;
af0 = params.af0;
El = params.El;
pp = params.pp;
```

```
%summing contributions from 48 lines (probably a lower number would suffice)
f=0;
w=0;
for i=1:1:48
a = (M.*a0(i)+(1-M).*af0(i)).*(p./p0).*(T0./T).^n(i);
st = s(i)*
(exp(-(h*c*El(i))/(kb*T))*
ppval(T0,pp)*
(1-exp(-(h*c*v02(i))/(kb*T))))/(exp(-(h*c*El(i))/(kb*T0))*
ppval(T,pp)*
(1-exp(-(h*c*v02(i))/(kb*T0))));
w = w+(l*NA*1)*(p/(R*T))*st.*((a)./(pi))./((v+offset-v0(i)).^2+(a).^2);
end
f=exp(-w); %final transmission
```

The function to extract spectralcalc data:

```
% Interpolates values from spectralcalc data.
% VMR must be given in percent
% T in Kelvin
% freq in gigahertz
function y = spectralcalc(T,VMR,freq)

c=3e8;
nu=freq*10^9; % Frequency in GHz
load('watersimulation.mat');
dataset2=dataset(:,:,:);
lambda = 10^6*c/nu; % Get lambda in microns
index = (lambda-600)/0.4+1; % Get index in the array corresponding to lambda
XI = VMR/5+1; % Get the index corresponding to VMR
YI = (T-373)/20+1; % Get the index corresponding to T
ZI = index;
y=interp3(dataset2,XI,YI,ZI); % Interpolation
```

B

Line data from HITRAN2008

Reference temperature T_0 for all T-dependent values is 293 K. Reference pressure 1 atm. Explanations:

- ν_0 is the frequency of the line center.
- S is the strength of the line at reference temperature.
- α_{air} foreign-broadened half-width due to collisions with air.
- α_{self} self-broadened half-width, i.e. broadening due to collisions between N_2 molecules.
- E_{lower} Energy of the lower state involved in the transition generating the line.
- n temperature-dependence exponent used in calculating line broadening.

Table B.1: Spectral lines of CO

$\nu_0[cm^{-1}]$	$S[cm^{-1}/(molecule - cm^{-2})]$	$\alpha_{air}[cm^{-1}/atm]$	$\alpha_{self}[cm^{-1}/atm]$	$E_{lower}[cm^{-1}]$	n
7.689917	2.552e-23	.0748	.0820	3.84500	.75
11.534513	8.210e-23	.0709	.0790	11.53490	.74
15.378665	1.820e-22	.0676	.0750	23.06940	.74
19.222222	3.262e-22	.0650	.0730	38.44810	.74
23.065059	5.075e-22	.0629	.0700	57.67030	.74
26.907008	7.117e-22	.0612	.0690	80.73530	.75
30.747929	9.206e-22	.0599	.0670	107.64230	.75
33.067177	1.126e-23	.0589	.0660	132.30500	.75
34.587674	1.114e-21	.0589	.0660	138.39030	.75
36.737059	1.299e-23	.0580	.0640	165.37220	.75
38.426099	1.275e-21	.0580	.0640	172.97790	.75

Table B.2: Spectral lines of water

$\nu_0[cm^{-1}]$	$S[cm^{-1}/(molecule - cm^{-2})]$	$\alpha_{air}[cm^{-1}/atm]$	$\alpha_{self}[cm^{-1}/atm]$	$E_{lower}[cm^{-1}]$	n
6.114567	7.785e-23	.0998	.5250	136.16390	.78
10.845940	9.105e-23	.0932	.5070	315.77950	.76
12.682023	8.304e-22	.0961	.6370	212.15640	.76
14.648500	7.145e-23	.0668	.3290	742.07630	.65
14.777502	1.483e-23	.0585	.2700	1045.05800	.62
14.943711	8.679e-22	.0871	.4670	285.41860	.71
15.707169	2.740e-23	.0692	.3460	742.07310	.69
15.833930	1.094e-22	.0764	.3960	488.13420	.70
16.294303	2.216e-23	.0854	.4870	586.47920	.76
18.268530	1.004e-22	.1039	.4860	23.75490	.77
18.413429	1.906e-23	.1039	.4860	23.77350	.77
18.577385	5.285e-20	.1039	.4860	23.79440	.77
20.704358	5.694e-22	.0803	.4190	488.10770	.81
21.948720	3.027e-23	.1035	.4680	1618.55710	.77
24.861210	6.689e-23	.1022	.4630	69.92740	.79
24.965870	1.264e-23	.1022	.4630	70.00470	.79
25.085124	3.483e-20	.1022	.4630	70.09080	.79
25.131090	1.383e-23	.1001	.4840	91.33020	.77
28.685368	1.912e-23	.1024	.4640	1664.96460	.72
29.808577	1.090e-23	.1013	.4770	0.00000	.78
30.227777	2.855e-23	.0792	.4160	1050.15770	.78
30.560189	1.433e-21	.0894	.4700	285.21930	.81
32.366233	1.609e-21	.0844	.4580	383.84250	.71
32.827305	1.835e-23	.0970	.4600	150.15620	.73
32.953690	2.532e-20	.1006	.4950	37.13710	.79
33.178791	5.098e-23	.1006	.4950	36.74860	.79
33.203354	1.440e-23	.0961	.4830	58.12690	.77
36.546242	3.185e-22	.1046	.5460	136.33670	.80
36.572472	5.995e-23	.1046	.5460	136.53760	.80
36.604150	1.645e-19	.1046	.5460	136.76170	.80
36.748650	9.702e-23	.0895	.5000	0.00000	.81
36.931110	1.831e-23	.0895	.5000	0.00000	.81
37.137125	5.042e-20	.0895	.5000	0.00000	.81
37.916370	3.414e-22	.0996	.5020	172.88290	.80
38.247168	1.135e-22	.0792	.4550	744.16270	.70
38.325691	6.482e-23	.0996	.5020	173.11010	.80
38.464169	2.543e-20	.0970	.5380	134.90160	.79
38.637531	2.440e-21	.0727	.4120	610.34120	.58
38.758568	2.174e-23	.0941	.4530	265.23620	.69
38.790556	1.793e-19	.0996	.5020	173.36580	.80
38.852543	2.422e-23	.0952	.4550	182.98350	.73
38.972245	1.107e-22	.0504	.2820	1216.19460	.44
39.111258	1.995e-22	.0628	.3040	888.63270	.49
39.407108	5.368e-23	.0970	.5380	133.47580	.79
39.656250	1.073e-22	.0925	.5000	274.80320	.83
39.721778	3.832e-23	.0554	.2950	1216.18980	.46
39.947941	2.030e-23	.0925	.5000	275.13050	.83
39.994469	9.178e-23	.1009	.4970	94.78870	.77

C

SpectralCalc simulations

The data downloaded from spectralcalc includes transmittance data for H_2O VMRs between 0% and 100% in steps of 5, temperatures between 373 K and 1073 K in steps of 20 and wavelengths from 600 to 1000 μm in steps of 0.4. The gas cell length is $L = 1$. This grid is fine enough to allow extraction of more precise values with MATLABs built-in *interp3* interpolation. We visualize relevant portions of the data below, first some representative spectra at varied T and VMR in figures C.1 and C.2. Then the ratio of the line strengths at the two strongest lines is plotted as functions of T and VMR respectively, shown in figures C.3 and C.4. We continue with the dependence of transmission on T and VMR at the two strongest waterlines in figures C.5 and C.6. Figures C.7 and C.8 shows plots of transmission as function of temperature for different VMR values. Correspondingly C.9 and C.10 show the transmission as function of VMR at fixed temperatures.

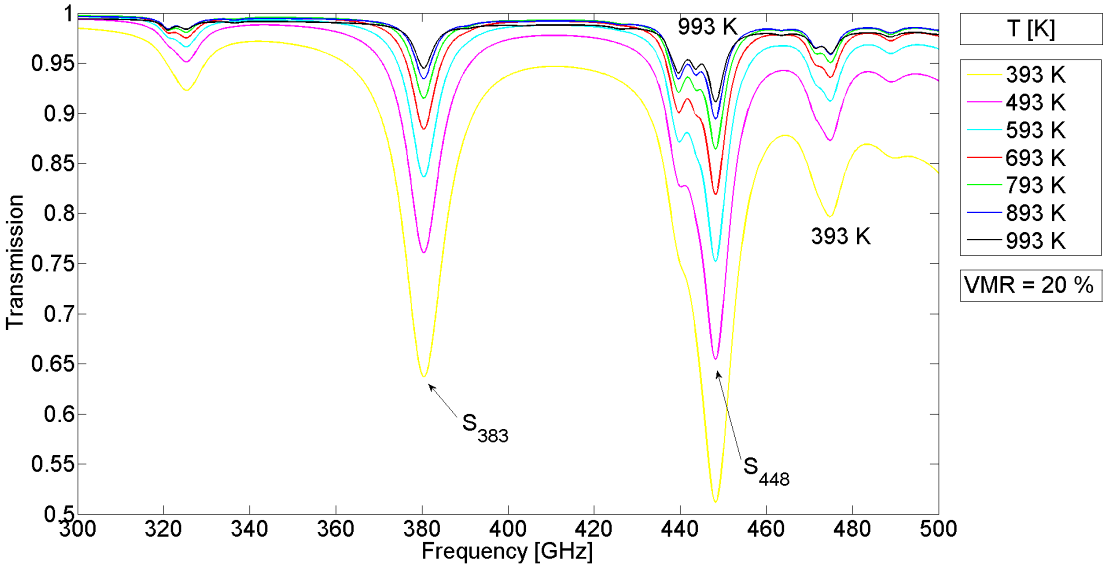

Figure C.1: The simulated spectra of H_2O at $VMR = 20\%$ and varying temperatures. [data/AppendixC]

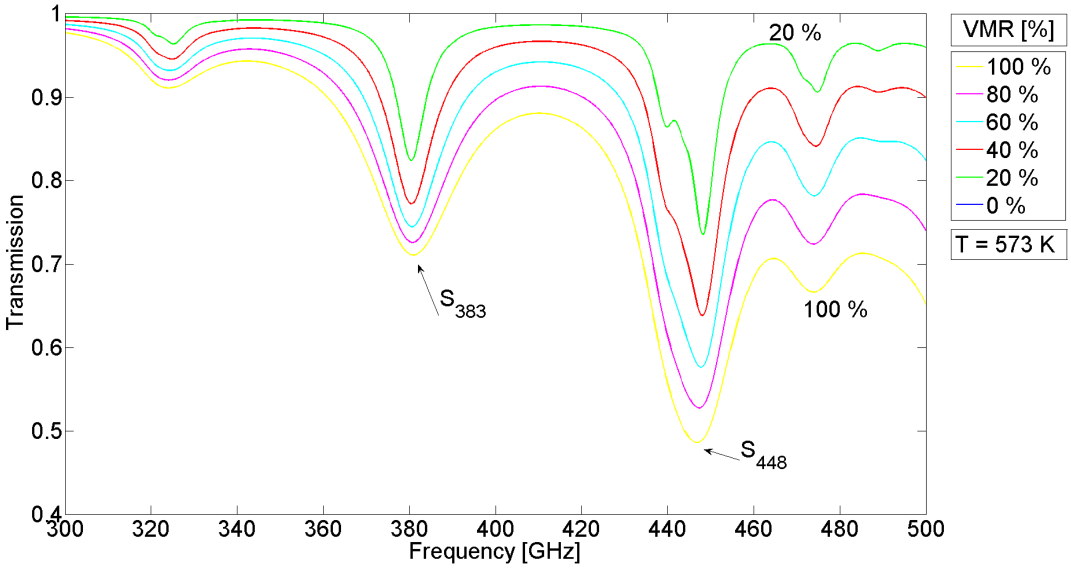

Figure C.2: The simulated spectra of H_2O at $T = 573K$ and varying humidity. [data/AppendixC]

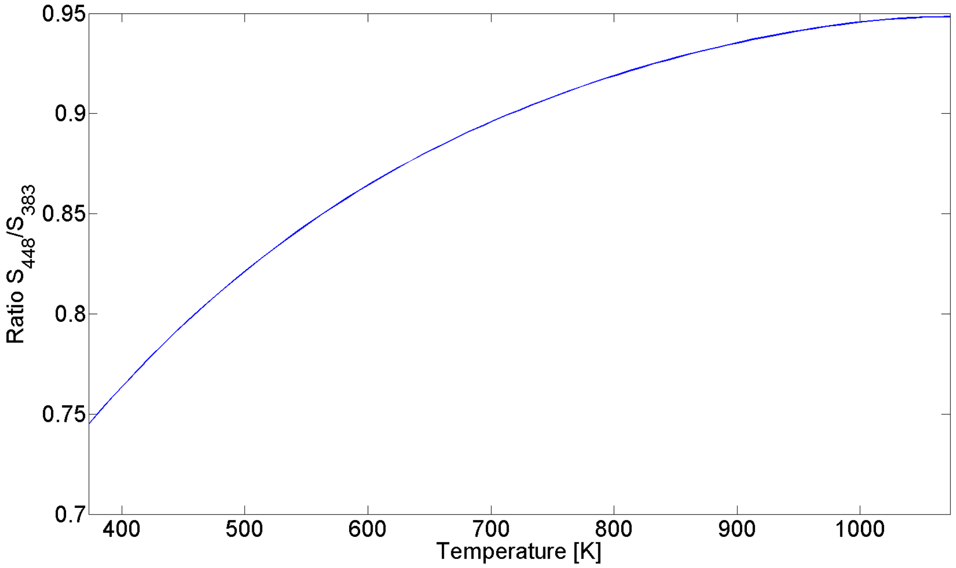

Figure C.3: Ratio of H_2O peak transmission at 448 and 383 as function of temperature when VMR is kept constant at 20%. [data/AppendixC]

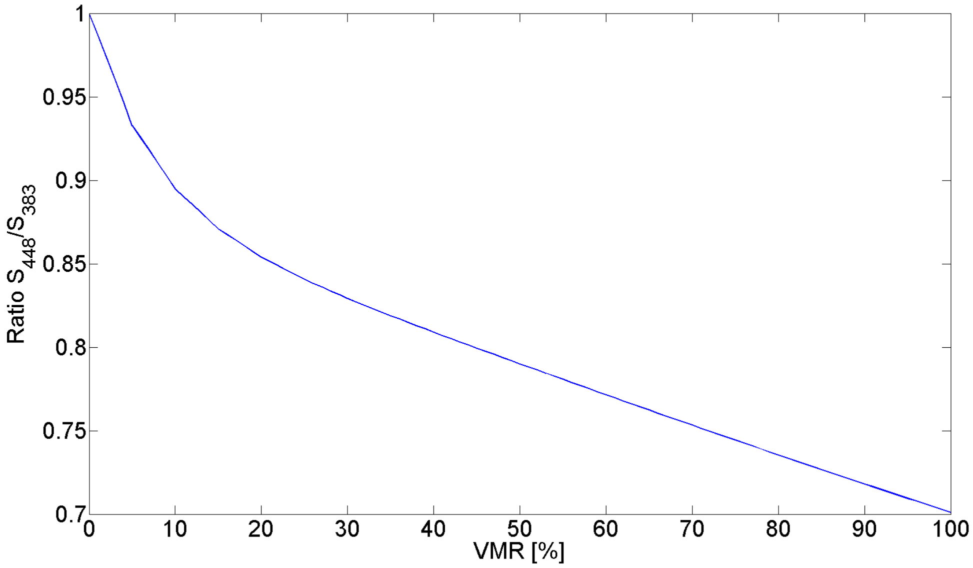

Figure C.4: Ratio of H_2O peak transmission at 448 and 383 as function of VMR when T is kept constant at 573 K. [data/AppendixC]

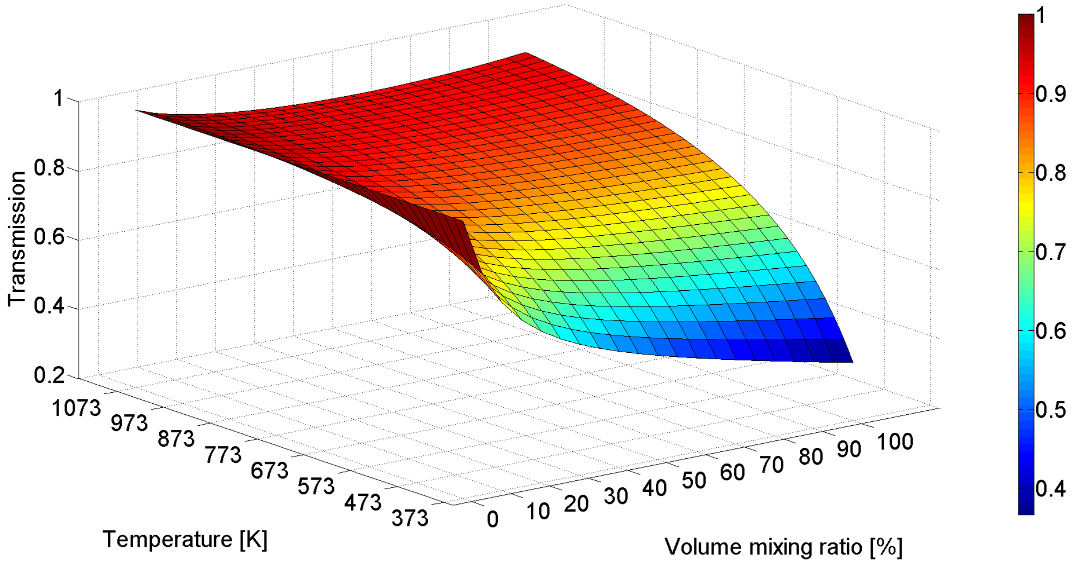

Figure C.5: The simulated transmission of H_2O at 380 GHz for various T and VMR. [data/AppendixC]

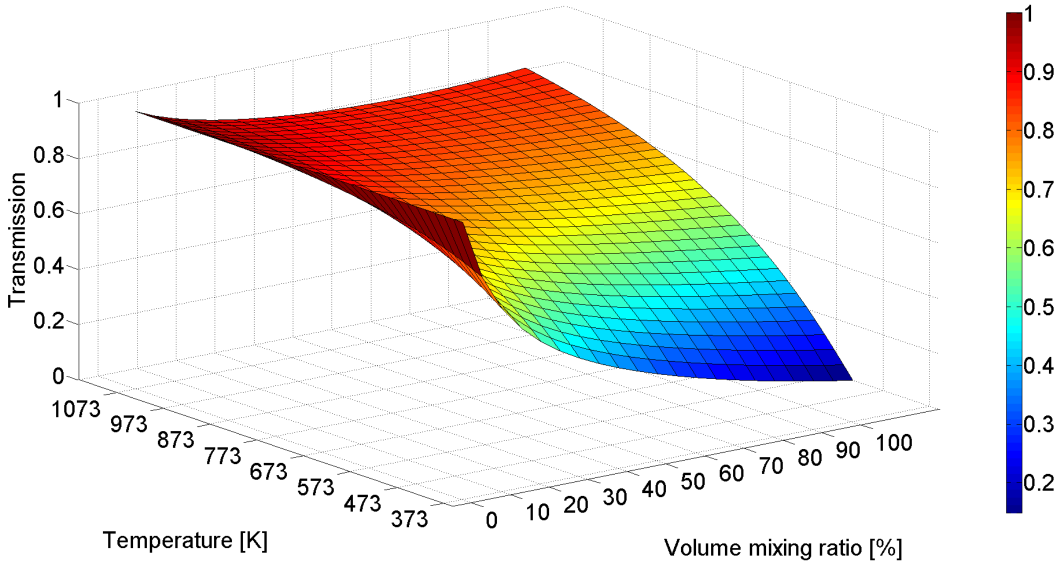

Figure C.6: The simulated transmission of H_2O at 448 GHz for various T and VMR. [data/AppendixC]

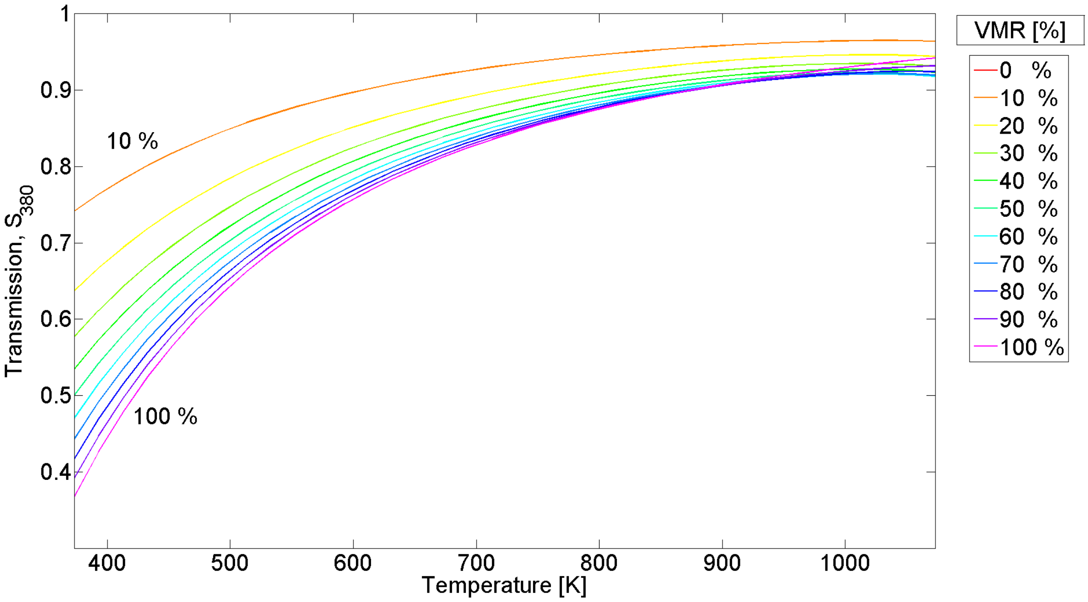

Figure C.7: The simulated transmission at 380 GHz, dependence on T for 10 different values of $H_2O\ VMR$. [data/AppendixC]

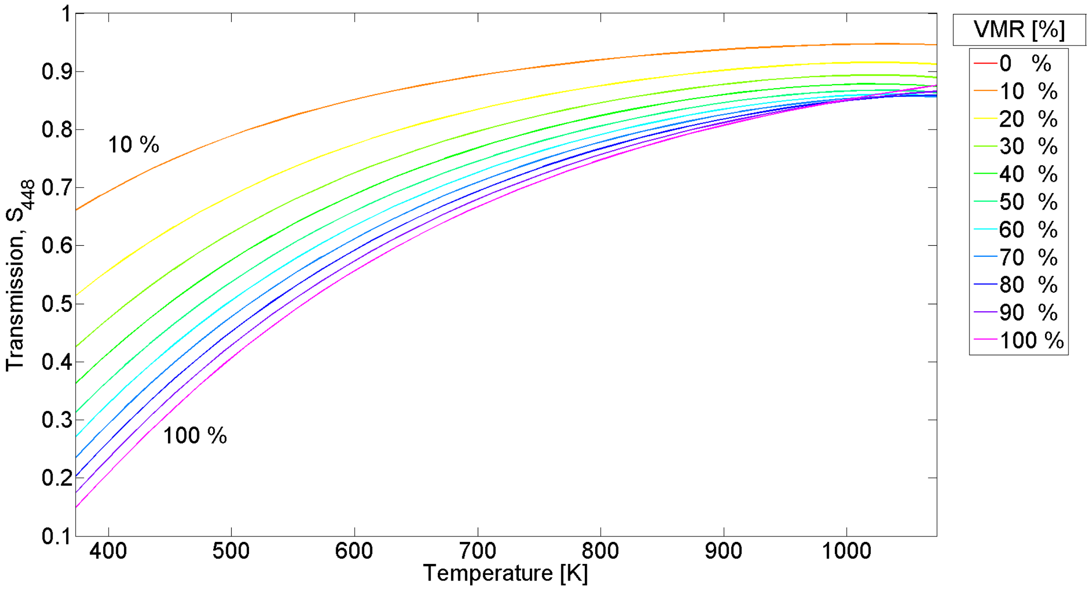

Figure C.8: The simulated transmission at 448 GHz, dependence on T for 10 different values of $H_2O\ VMR$. [data/AppendixC]

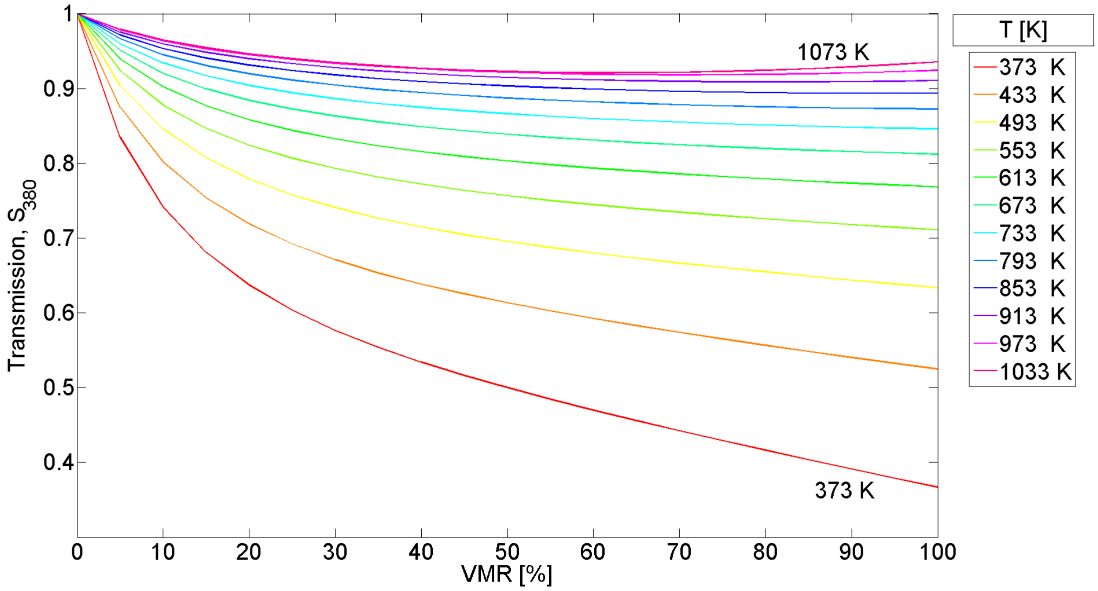

Figure C.9: The simulated transmission at 380 GHz, dependence on $H_2O\ VMR$ for 12 different values of T. [data/AppendixC]

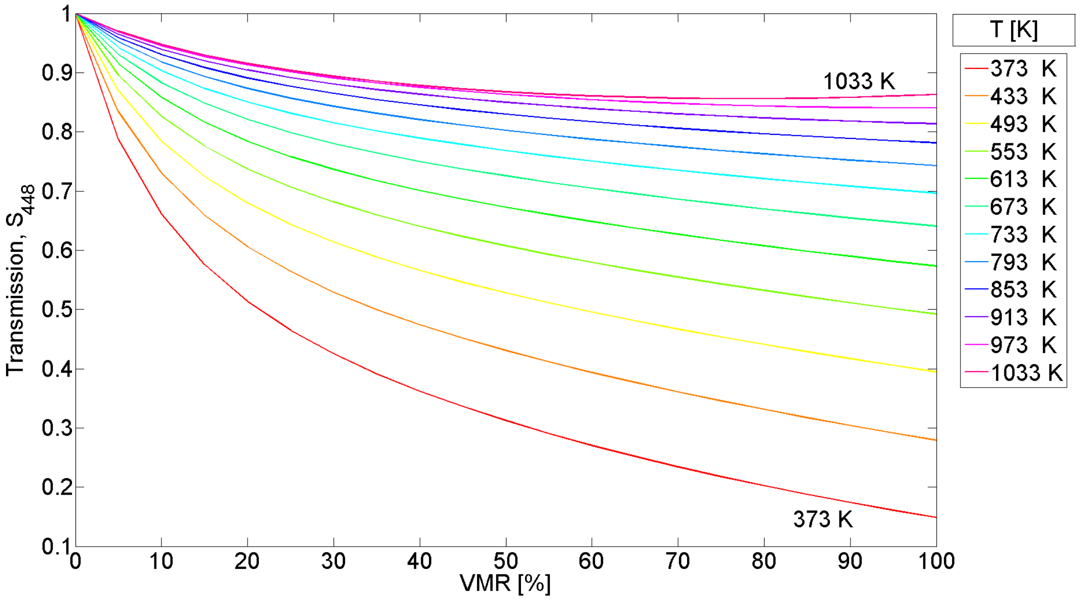

Figure C.10: The simulated transmission at 448 GHz, dependence on $H_2O\ VMR$ for 12 different values of T. [data/AppendixC]

D

Calculations of T and VMR from S_{380} and S_{448}

D.1 Determination of T from measured VMR and S

For estimating temperatures corresponding to the data in table 4.1, with results shown in table 5.1, the following MATLAB code was used.

```
t380=[0.784,0.8,0.813,0.822,0.825,0.824,0.819,0.792];
%Transmission at 380 GHz
err380=[0.00428,0.00519,0.00502,0.00527,0.00509,0.00366,0.00259,0.00261];
%Standard deviation at 380 GHz
t448=[0.684,0.721,0.751,0.774,0.781,0.786,0.76,0.73];
%Transmission at 448 GHz
err448=[0.00870,0.00921,0.00836,0.00838,0.00830,0.00692,0.00979,0.00792];
%Standard deviation at 448 GHz
hum=[0.95,0.73,0.57,0.48,0.41,0.49,0.57,0.73];
%Humidity level, VMR [%]
errhum=[0.0152,0.0099,0.011,0.011,0.0077,0.0119,0.0084,0.009];
%Standard deviation of humidity level, %
global T380 T448 D380 D448;
for n=1:1:8
T(n)=fitT(t380(n),t448(n),hum(n),err380(n),err448(n),errhum(n))+373;
Tat448(n)=T448; %T at the 448 line
Tat380(n)=T380; %T at the 380 line
T2(n)=(Tat448(n)+Tat380(n))/2;%temperature
Dat448(n)=D448; %error at the 448 line
Dat380(n)=D380; %error at the 380 line
```

```
diff2(n)=(Dat448(n)+Dat380(n))/2;%Standard deviation of T
n
end

T2
Tat448
Tat380

diff2
Dat448
Dat380
```

where the function ”fitT” is given by:

```
function y=fitT(t380,t448,hum,err380,err448,errhum)

global offset params D T380 T448 D380 D448;
offset=0;
params=load('waterlinedata4.mat');
plot380=zeros(1,1073);
plot448=zeros(1,1073);
hum2=hum*100;
for T=373:1:1073
%plot448(T)=trans([T,hum],448);
plot448(T)=spectralcalc(T,hum2,448);
%plot380(T)=trans([T,hum],383);
plot380(T)=spectralcalc(T,hum2,383);
error380(T)=(t380-plot380(T))^2;
error448(T)=(t448-plot448(T))^2;
error(T)= (t380-plot380(T))^2+(t448-plot448(T))^2;
end
[C y]=min(error(373:1073));
z=y+373;
[C448 y448]=min(error448(373:1073));
T448=y448+373;
[C380 y380]=min(error380(373:1073));
T380=y380+373;
D448=((z+10)-(z-10))/(plot448(z+10)-plot448(z-10))*err448;
D380=((z+10)-(z-10))/(plot380(z+10)-plot380(z-10))*err380;
```

and the function ”trans” is given in appendix A.

D.2 Determination of VMR from calculated T and measured S

For estimating VMR from calculated temperatures in 4.1, with results shown in table 5.1, the following MATLAB code was used.

```
t448=[0.684,0.721,0.751,0.774,0.781,0.786,0.76,0.73];
%Transmission at 448 GHz
err448=[0.00870,0.00921,0.00836,0.00838,0.00830,0.00692,0.00979,0.00792];
%Standard deviation at 448 GHz
err380=[0.00428,0.00519,0.00502,0.00527,0.00509,0.00366,0.00259,0.00261];
%Standard deviation at 380 GHz
t380=[0.784,0.8,0.813,0.822,0.825,0.824,0.819,0.792];
%Transmission at 380 GHz
hum=[0.95,0.73,0.57,0.48,0.41,0.49,0.57,0.73];
%Temperatures, calculated.
errT=[4.9039,6.5779,7.2988,8.5231,8.9266,6.8196,6.6685,4.6595];
%Stanbdard deviation of temperatures.
global D;
for n=1:1:8
VMR(n)=fitVMR(t380(n),t448(n),T(n),err380(n),err448(n),errT(n));
diff(n)=D; %Standard deviation of T
end
VMR
diff
```

where the function "fitVMR" is given by:

```
function y=fitVMR(t380,t448,T,err380,err448,errT)

global offset params D;
offset=0;
params=load('waterlinedata4.mat');
plot380=zeros(1,100);
plot448=zeros(1,100);
for hum=1:1:100
plot448(hum)=trans([T,hum/100],448);
plot380(hum)=trans([T,hum/100],380);
error(hum)= (t380-plot380(hum))^2+(t448-plot448(hum))^2;
end
[C y]=min(error(1:100));
z=y/100;
D=(1/2)*(((y+1)-(y-1))/(plot448(y+1)-plot448(y-1))*err448+((y+1)-(y-1))/(plot380(y+1)-plo
```

and the function ”trans” is given in appendix A.

D.3 Simultaneous determination of T and VMR from S

This does not work with only two lines, it is conjenctured that measuring another line could make it work though.

```
t448=[0.684,0.721,0.751,0.774,0.781,0.786,0.76,0.73];
%Transmission at 448 GHz
err448=[0.00870,0.00921,0.00836,0.00838,0.00830,0.00692,0.00979,0.00792];
%Standard deviation at 448 GHz
err380=[0.00428,0.00519,0.00502,0.00527,0.00509,0.00366,0.00259,0.00261];
%Standard deviation at 380 GHz
t380=[0.784,0.8,0.813,0.822,0.825,0.824,0.819,0.792];
%Transmission at 380 GHz
hum=[0.95,0.73,0.57,0.48,0.41,0.49,0.57,0.73];
%Temperatures, calculated.
errT=[4.9039,6.5779,7.2988,8.5231,8.9266,6.8196,6.6685,4.6595];
%Stanbdard deviation of temperatures.
global D;
for n=1:1:8
[T(n),VMR(n)]=fitBoth(t380(n),t448(n));
end
T
VMR
```

Where ”fitBoth” is given by:

```
% Fits using a stepsize of 10 for T and 0.05 for VMR.
function [x,y]=fitBoth(t380,t448)

global offset params;
offset=0;
params=load('waterlinedata4.mat');
plot380=zeros(21,71);
plot448=zeros(21,71);
for T=1:1:71
    for hum=1:1:21
    plot448(T,hum)=trans([(T*10+363),(hum*0.05-0.05)],448);
    plot380(T,hum)=trans([(T*10+363),(hum*0.05-0.05)],380);
    error(T,hum)= (t448-plot448(T,hum))^2+(t380-plot380(T,hum))^2;
    end
end
```

```
[r,c]=find(error==min(min(error))); %Finding the minimum of a 2D array.
x=363+r*10 % Converting the temperature from steps to K.
y=(c-1)*0.05 % Converting VMR from steps to ratio.
```

E

Humidity control

The humidifier (Cellkraft E-1000 precision evaporator) is controlled via buttons that increase or decrease target water consumption in steps of 0.01 g. The VMR of H_2O is determined by the combination of vaporization rate with the flow rate of the N_2 into which the steam is injected. The setting on the humidifier is unfortunately not well calibrated and external measurement of water consumption is needed. For this a digital scale (Ohaus Scout Pro) was used. When the consumption of water as well as the flow of N_2 are known, one can determine the VMR as follows. We start with the ideal gas equation:

$$pV = nRT \tag{E.1}$$

where P is gas pressure, V is volume, n is amount of substance in moles, R is the ideal gas constant and T is temperature. We control the volume of N_2 entering the system per unit time. We also know that volumetric ratio is determined på molar ratio, so we calculate the number of moles entering the system:

$$n = \frac{p}{RT}V \rightarrow n = \frac{101325}{8.314 \cdot 293.15}V \rightarrow n = 41.57V \tag{E.2}$$

where V has the unit of m^3. At 100% flow rate our flow is 5 L/min so we get $n = 0.005 \cdot 41.57 \cdot FL_{N_2} = 0.2079 \cdot FL_{N_2}$ mol/min.

$$VMR_{H_2O} = \frac{FL_{H_2O}/M_{H_2O}}{(0.01 \cdot FL_{N_2} \cdot 0.2079) + (FL_{H_2O}/M_{H_2O})} \tag{E.3}$$

where FL_{H_2O} is given in g/min, FL_{N_2} in % on the mass flow controller and $M_{H_2O} = 18.0148$ g/mol.

F

Alternative waveguides

Some alternative waveguides were tested with regard to their attenuation properties. No such tests with gas were conducted. The table F.1 shows the different waveguides and their attenuation.

Table F.1: Transmission at three distances with and without waveguide, normalized to the 10 cm air transmission.

medium	I at 10 cm	I at 20 cm	I at 30 cm
air	1.00	0.799	0.687
7 mm copper tube	0.0578	0.0176	0.0119

Index